EUROPEAN Journal of Molecular Biotechnology

Has been issued since 2013.
E-ISSN 2409-1332
2018. 6(2). Issued 2 times a year

Journal is indexed by: **Chemical Abstracts Service** (USA), **CiteFactor** – Directory of International Reseach Journals (Canada), **Cross Ref** (UK), **EBSCOhost Electronic Journals Service** (USA), **Global Impact Factor** (Australia), **Journal Index** (USA), **Electronic scientific library** (Russian Federation), **Open Academic Journals Index** (USA), **Sherpa Romeo** (Spain), **ULRICH's WEB** (USA).

All manuscripts are peer reviewed by experts in the respective field. Authors of the manuscripts bear responsibility for their content, credibility and reliability.

Editorial board doesn't expect the manuscripts' authors to always agree with its opinion.

Postal Address: 1367/4, Stara Vajnorska str., Bratislava – Nove Mesto, Slovakia, 831 04

Website: http://ejournal8.com/
E-mail: aphr2010@mail.ru

Founder and Editor: Academic Publishing House Researcher s.r.o.

Release date 15.12.18.
Format 21 × 29,7/4.

Headset Georgia.

Order № 18.

European Journal of Molecular Biotechnology

2018

Is. 2

C O N T E N T S

Articles and Statements

Published in the Slovak Republic
European Journal of Molecular Biotechnology
Has been issued since 2013.
E-ISSN: 2409-1332
2018, 6(2): 69-75

DOI: 10.13187/ejmb.2018.2.69
www.ejournal8.com

Articles and Statements

Natural Bond Order Analysis of HCN→HNC Isomerization Mechanism in the Interstellar Clouds Conditions: DFT Investigation

Abdelilah Benallou [a, *]

[a] University Chouaib Doukkali, El Jadida, Morocco

Abstract

The optimum geometries and quadratic force constants of HCN, HNC, intermediates (INT1 and INT2) and the transition state connecting them (CHN) have been determined at the DFT (density functional theory) level of theory. Energy differences were evaluated using the DFT method in conjunction with 6-311++g(d,p) basis set. The most reliable structure obtained for the transition state has bond distances of 1.184, 1.193 and 1.391Å for r_{CN}, r_{CH} and r_{NH}, respectively. Including a correction for zero-point vibrational energies, the transition state activation energy is predicted to be 44.6kcal/mol. So the transition state of isomerization pathway is highly energetic and subsequently cannot occur efficiently in the gas phase.

Keywords: isomerization, DFT, HCN, Zero point energy, Gas phase.

1. Introduction

HCN and HNC molecules are of great interest in astronomy. They have been observed in many galactic and extragalactic objects, ranging from circumstellar masers through interstellar clouds to planetary atmospheres. The role of hydrogen cyanide (HCN) in the prebiotic formation of primitive nucleobases and amino acids has been studied for decades (Oro, 1961; Kliss et al., 1962; Chakrabarti et al., 2000; Glaser et al., 2007; Roy et al., 2007; Ferris et al., 1984; Rehder, 2010; Ghosh et al., 1980; Smith et al., 2001; Kikuchi et al., 2000; Hughes, 2009; Benallou, 2016; Benallou, 2017; Benallou, 2017). The interconversion of hydrocyanic and hydroisocyanic acids (HCN and HNC, respectively) is arguably one of the simplest isomerization processes in all of the chemistry. The former isomer is more stable thermodynamically, and presents the dominant form found on Earth. However, the isomeric ratio in deep space is not under thermodynamic control, and the abundance of the less stable form (HNC) is comparable to that of HCN (and in fact exceeds that of HCN along certain lines of sight). The HCN/HNC interconversion has been extensively studied both experimentally and theoretically.

The purpose of this study to a new and accurate estimate the HCN/HNC isomerization process as it proceeds via a straightforward proton transfer mechanism. Given the simplicity of the system, the mechanism of the HCN→HNC isomerization is so rarely studied by the new method in which having used the electronic correlation in their calculation. In our work, we will try to investigate the different pathway of the isomerization

* Corresponding author
E-mail addresses: abdo_benallou@yahoo.fr (A. Benallou)

mechanism of compound HCN in the interstellar clouds conditions in order to study the probability of prebiotic formation in earth conditions.

2. Computational methods

The geometry of the complexes has been optimized with B3LYP/6-311++G** (Becke, 1993; Lee et al., 1988; Hariharan et al., 1973) computational methods. All the calculations were performed with the GAUSSIAN G09 program package (Frisch et al., 2009). The electronic structures are analyzed at the stationary point by using the NBO (natural bond orbital) method (Benallou et al., 2015; Benallou et al., 2016; Glendering et al., 1998). The minima or transition state nature of the complexes has been established based on the sign of the harmonic vibrational frequencies calculated at the B3LYP/6-311++G** level using the geometries obtained at the corresponding computational levels. The interaction energy of the complexes has been calculated as the difference between the total energy of the complexes and those of the isolated monomers**.**

3. Results and discussion

3.1. HCN, CHN and HNC isomers formation mechanism

The DFT optimized structures, of CHN, HCN and HNC are presented in Figure 1. Analyst's structures of HCN to HNC isomerization of DFT method give a reliable comprehension of the mechanism reaction, the reaction of HCN isomerization has three stationary points in which two intermediates and a transition state characterized by a single imaginary frequency as we noted in figure 1. However, we noticed that the equilibrium distance between atoms of HCN is about 1.066Å for H–C and 1,149Å for C–N in good agreement with experimental values (1.065 and 1.153Å) (Herzberg, 1966) as well for intermediate CHN (INT1) the proton did a rotation about the CN bond of an angle to 80.241° in such that the distance of this bond is changed to 1.156Å, so the H proton will move from carbon to nitrogen atom correspond to an extension to the C–N bond to 1.181Å. TS or CHN will be determined by the negative vibration frequency of Hessian matrix, in which the imaginary frequency to be -1127,3259cm^{-1}, thus their geometry illustrate that the proton is positioned closer to C atom than that nitrogen N in such the H–C distance is 1.193Å (against 1.392Å of H–N), as long as the CN bond has been increased slightly to 1.184Å, this latter bond is unsaturated and still triple form (C≡N), HCN and HNC angles are very acute, especially from HNC in which has a value of 54° degree, the geometry of the intermediate 2 (CHN2) show that the final shift from the proton (H) of the carbon to nitrogen atom is at this monomers because the distance between H and N becomes very short to be 1.079Å, at this INT2 the C–N distance becomes longer to be 1.202Å in which mean that this bond becomes feeble. In the HNC isomer, the HN bond becomes stronger than that HC of the HCN isomer such as its distance will be 1.000Å (against 1.066Å from HC) and the CN distance becomes longer than that of the starting HCN isomer (1.149Å to 1.169Å) and are very similar to experimental results r(NH)=0.986 and r(CN)=1.173Å (Harmony et al., 1979), so HNC isomer is less stable than HCN isomer. Subsequently, these results strongly indicate that DFT calculations are in consistency with the experimental results.

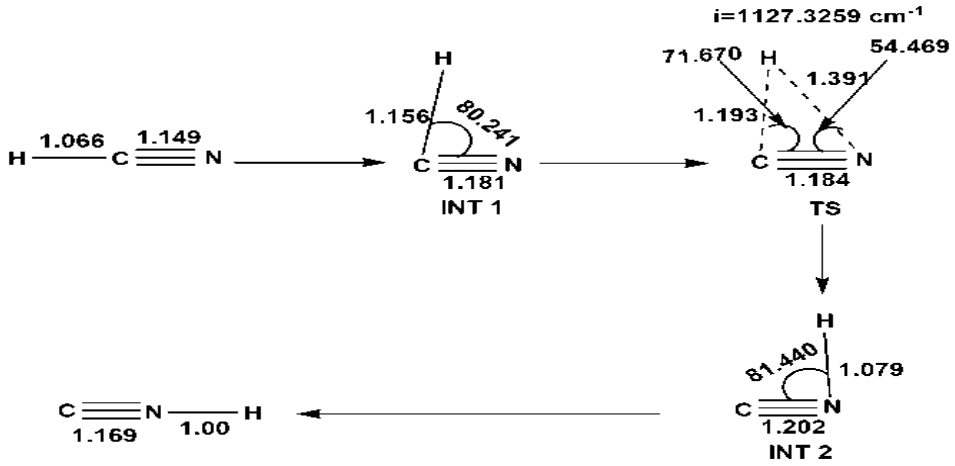

Fig. 1. Isomerization pathway calculated on the DFT method in the 6-311++(d,p) basis set, angles are given in degree and distances in Å

After the location of the maximum point (transition state), hence we can know whether that the latter (TS) connect the two minima HCN and HNC isomers by IRC (Intrinsic reaction coordinate) calculation of the transition state at several points of the isomerization process as shown in Figure 2.

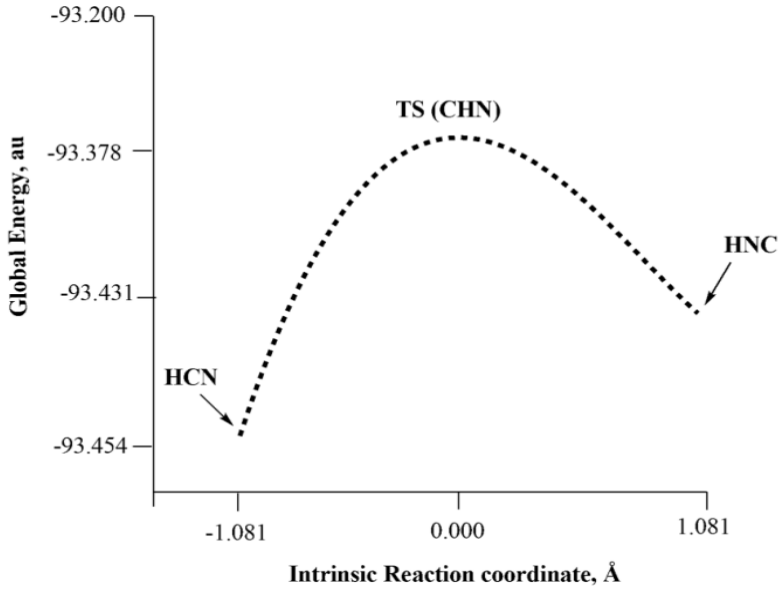

Fig. 2. Intrinsic reaction coordinates of HCN/HNC isomerization

The analysis of Figure 2 confirms that this transition state is totally verified the isomerization process such as that mechanism passes principally by three stationary points, two minima (HCN and HNC) and a maximum (CHN; TS).

In order to evaluate the progress of the HCN→HNC isomerization and H–C, C–N and H–N bond orders, we calculated the Wiberg index (Wiberg, 1968) by using the NBO (natural bond order) analysis, the found results are displayed in Table 1.

Table 1. Wiberg index of H–C, C–N and N–H bonds calculated to the HCN, HNC and the connecting transition state (CHN)

Species	H-C	C-N	N-H
HCN	0.9363	2.9907	0.0181
CHN	0.5822	2.5856	0.3191
HNC	0.0310	2.4746	0.7841

Bond orders calculated using the Wiberg index are helped us to note that the C–H bond goes through a cycle of destruction or breaking process such as the bond orders become very small when going from HCN to HNC of 0.9363 to 0.0310 as well the N–H bond is strengthened and becomes very short in such the bond order was increased from 0.0181 (HCN) to 0.7841 (HNC) that meaning NH is finally formed, while C–N bond order is slightly reduced to be 2.9907 to 2.4746 in which this bond has been extended but does not break. Therefore, this result gives a reliable conclusion of isomerization process in which HCN will be transformed theoretically to HNC isomer in the gas phase.

3.2. Energy difference between HCN and HNC and then the energy difference between HCN and CHN isomers

The global energies of the HCN, HNC and CHN stationary points, obtained with the DFT electron-correlation method at 6-311++(d,p) basis sets, are portrayed in Table 2.

Table 2. Global energy (E) in (au) of HCN, INT1, CHN (TS), INT2 and HNC species calculated on DFT method at 298K

HCN	INT1	CHN	INT2	HNC
-93.454	-93.380	-93.378	-93.395	-93.431

au: atomic units

The global energies calculated on the DFT method demonstrate that HCN is the most energetic species and the transition state (TS) has a less energy compared with other species such as we have found for HCN, -93.4545au and for TS, -93.3780au, therefore the HCN isomer is more stable to that of HNC in which HNC-HCN energy difference is noticeably positive, 14.432kcal/mol. Consequently, this isomerization process is energetically endothermic and thus the HCN→HNC process ongoing from stable to unstable state, therefore HNC isomer can be dissociated easily in the presence of another chemical compound.

In order to determinate the vibrational energy related to the HCN, CHN and HNC species at 0°C we have calculated the zero point energy (ZPE) of these species, the results are dipected in Table 3.

Table 3. Zero point energy (ZPE) of HCN, CHN and HNC species

	HCN	CHN	HNC
ZPE(kcal/mol)	10.265	6.658	9.861

We have seen that the ZPE energy of HCN, CHN, and HNC species at 0°C has been known an increase toward the stability of these species, such as the transition state (CHN) that has the lowest energy of ZPE to be 6.658 kcal/mol in which less stable compared to the other isomers. Equally, HNC isomer that is less stable than HCN has an average value of ZPE to be 9.861 kcal/mol. Therefore, the greatest value of ZPE energy is belonging to the most stable isomer in such HCN of 10.265 kcal/mol. Thus, ZPE identification of each species we help us to calculate the thermodynamic energy at 298K, the results are given in Figure 3. The zero point energy has been included carefully to these energies.

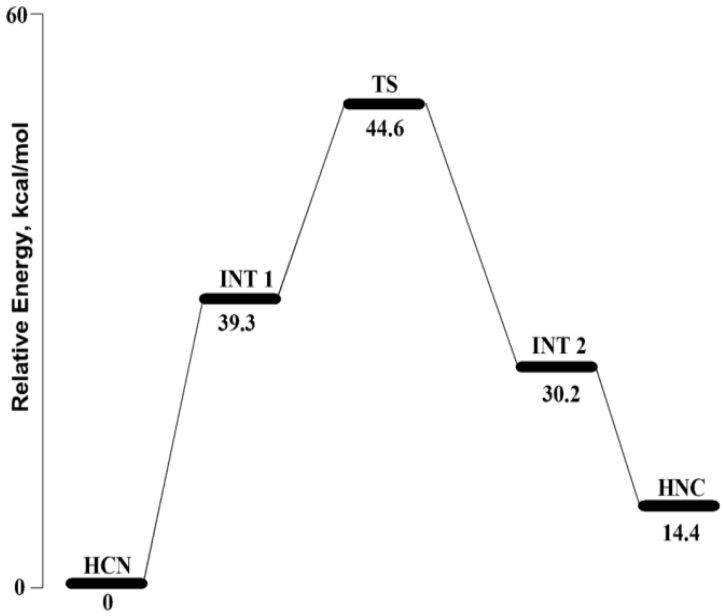

Fig. 3. Profile energetic in kcal/mol, of the HCN→HNC isomerization process

The mentioned results in Figure 3 show that the relative energy (E), calculated using the DFT method is sufficiently positive and greater than 0kcal/mol. Therefore, this isomerization process is endothermic. However, HCN isomerization ongoing through the barrier energy of 44.6 kcal/mol to likely takes place. In addition, the isomerization process passes through two intermediates, in which the first intermediate 1 (39.3 kcal/mol) is essential for HCN shifts to the CHN (TS) and the second intermediate 2 (30.2 kcal/mol) is necessary for CHN take place to the final HNC compound (14.4 kcal/mol) in agreement with the calculation of energies barrier of the intermediate 1 and 2 in which the activation energy are Ea (INT2) < Ea (INT1) < Ea (TS).

So the isomerization pathway is done as follows: HCN→INT2 (proton rotation around of the carbon)→CHN (the proton moves between the carbon and nitrogen atoms)→INT2 (proton shifts from carbon to the nitrogen atom)→ HNC.

In order to identifying the charge transfer between H, C, and N atoms in the studied isomers, we will be calculated the Mulliken charge, the results are given in Table 4.

Table 4. Atomic charge of Mulliken (*e*) calculated by DFT method

Atoms	HCN	CHN	HNC
H	0.175522	0.214231	0.278070
C	0.063687	-0.182765	-0.157088
N	-0.239209	-0.031466	-0.120983

In Table 4, we have remarked that the H proton has a perceptible positive charge in the beginning of the reaction will acquire an electrophilic character because has lost many important charge along the isomerization process to become more electrophilic; 0.175522*e* from HCN to 0.278070*e* of HNC. However, the carbon atom that has previously positive charge in HCN to be 0.063687*e* which took a negative charge at CHN and HNC isomers, -0.182765*e* and -0.157088*e*, respectively. Subsequently, the carbon atom has accepted more electronic charge from nitrogen and hydrogen atoms in which take more nucleophilic character (HC bond breaking) as well the nitrogen atom was negative charge in HCN isomer will lose many considerable charges during the isomerization process as in CHN and HNC isomers (charge transferred principally to the carbon atom).

4. Conclusion

The HCN and HNC isomers and the transition state connecting them (CHN) have been studied using DFT method theory. The optimum geometries and harmonic frequencies of the HCN, HNC and CHN stationary points have been determined at the 6-311++(d,p) basis set level. The isomerization process involved two intermediates in which INT1 and INT2 and a transition state connecting the HCN to HNC. The energy difference (ΔE) between HCN and HNC and the energy difference (Ea) between HCN and CHN have been evaluated. The best estimates for ΔE and Ea obtained in this work are 14.4 kcal/mol and 44.6 kcal/mol respectively. The results of this study show that the isomerization process is thermodynamically endothermic and needing more energy from external source to likely takes place in the gas phase of interstellar clouds.

References

Oró, 1961 – *Oró, J.* (1961). Mechanism of synthesis of adenine from hydrogen cyanide under possible primitive earth conditions. *Nature*. 191, 1193.

Kliss, Matthews, 1962 – *Kliss, R.M., Matthews, C.N.* (1962). Hydrogen cyanide dimer and chemical evolution. *Proc. Natl. Acad. Sci.* 48, 1300.

Chakrabarti, Chakrabarti, 2000 – *Chakrabarti, S., Chakrabarti, S.K.* (2000). Can DNA bases be produced during molecular cloud collapse? *Astron. Astrophys*. 354, l6.

Glaser et al., 2007 – *Glaser, R., Hodgen, B., Farrelly, D., Mckee, E.* (2007). Adenine synthesis in interstellar space: mechanisms of prebiotic pyrimidine-ring formation of monocyclic HCN-pentamers. *Astrobiology*. 7, 455.

Roy et al., 2007 – *Roy, D., Najafian, K., Von ragué, Schleyer P.* (2007). Chemical evolution: the mechanism of the formation of adenine under prebiotic conditions. *Proc. Natl. Acad. Sci.* 104, 17272.

Ferris, Hagan, 1984 – *Ferris, J.P., Hagan, W.J.* (1984). HCN and chemical evolution: the possible role of cyano compounds in prebiotic synthesis. *Tetrahedron*. 40, 1093.

Rehder, 2010 – *Rehder, D.* (2010). Chemisty in space: from interstellar matter to the origin of life, (ed.). *Wiley VCH,* weinheim.

Ghosh, Ghosh, 1980 – *Ghosh, K.K., Ghosh, S.N.* (1980). A mechanism for the formation of glycine, adenine and guanine in interstellar space. *Life. Sci. Space. Res*. 18, 37.

Smith et al., 2001 – *Smith I.W.M., Talbi D., Herbst E.* (2001). The production of HCN dimer and more complex oligomers in dense interstellar clouds, *Astron. Astrophys*. 369, 611.

Kikuchi et al., 2000 – *Kikuchi, O., Watanabe, T., Satoh, Y., Inadomi, Y.* (2000). Ab initio GB study of prebiotic synthesis of purine precursors from aqueous. hydrogen cyanide: dimerization reaction of HCN in aqueous solution, *J. Mol. Struct. (Theochem.)*. 507, 53.

Hughes, 2009 – *Hughes, A.B.* (2009). Amino acids, peptides and proteins in organic chemistry: Vol.1 origins and synthesis of amino acids, (ed.), *Wiley-VCH,* Weinheim.

Benallou et al., 2016 – *Benallou, A.* (2016). Understanding the most favourable dimer of HCN for the oligomerization process in the gas phase of interstellar clouds. *Comp. Theo. Chem*. 1097, 79.

Benallou et al., 2017 – *Benallou, A.* (2017). The mechanism determination of trimer and tetramer HCN for adenine formation in the gas phase of interstellar space. *Comp. Theo. Chem*. 1101, 68.

Benallou et al., 2017 – *Benallou, A.* (2017). Understanding the temperature and pressure role of HCN→HNC isomerization as well as vibrational and rotational energies of these species. *Arab. Phys. Chem*. 4, 1.

Becke, 1993 – *Becke, A.D.* (1993). Density-functional thermochemistry. III. The role of exact exchange. *J. Chem. Phys*. 98, 5648.

Lee et al., 1988 – *Lee, C., Yang, W., Parr, R.G.* (1988). Development of the colle-salvetti correlation-energy formula into a functional of the electron density. *Phys. Rev. B*. 37, 785.

Hariharan, Pople, 1973 – *Hariharan, P.A., Pople, J.A.* (1973). The influence of polarization functions on molecular orbital hydrogenation energies. *Theor. Chim. Acta*. 28, 213.

Frisch et al., 2009 – *Frisch, M.J., et al.* (2009). Gaussian 09, Revision A.02, Gaussian, Inc., Wallingford, CT.

Benallou et al., 2015 – *Benallou, A., Garmes, H., El, abdallaoui H.E.* (2015). GIAO calculations of chemical shifts of NMR spectra of 1H and 13C of the hexahydroindoles products. *Mor. J. Chem*. 3, 238.

Benallou et al., 2016 – *Benallou, A., Garmes, H., El abdallaoui, H.E.* (2016). Effect of hydrogen bonding on the intramolecular cycloaddition Diels-Alder reaction of triene-amide in an aqueous solution (case of a single molecule of water). *Tetrahedron*. 72, 76.

Glendering et al., 1998 – *Glendering, E.D., Reed, A.E., Carpenter, J.E., Weinhold, F.* (1998). NBO. Ver.3.1. Tci. *University of Wisconsin*. Madison.

Herzberg, 1966 – *Herzberg, G.* (1966). Electronic spectra and electronic structures of polyatomic molecules. *Van Nostrand*, New York.

Harmony et al., 1979 – *Harmony, M.D., Laurie, V.W., Kuckzowski, R.L., Schwendeman, R.H., Ramsay, D.A., Lovas, F.J., Lafferty, W.J., Maki, A.G.* (1979). Molecular structures of gas-phase polyatomic molecules determined by spectroscopic methods. *J. Phys. Chem. Ref. Data*. 8, 619.

Wiberg, 1968 – *Wiberg, K.B.* (1968). Application of the pople-santry-segal CNDO method to the cyclopropylcarbinyl and cyclobutyl cation and to bicyclobutane. *Tetrahedron*. 24, 1083.

Published in the Slovak Republic
European Journal of Molecular Biotechnology
Has been issued since 2013.
E-ISSN: 2409-1332
2018, 6(2): 76-82

DOI: 10.13187/ejmb.2018.2.76
www.ejournal8.com

Manganese- and Zinc-Containing Metalloproteins Have a Value in the Species Composition of Semi-Artificial Arid Phytocenoses in the Contact Zone with the Agrocenoses

Valery V. Novochadov [a, *], Pavel A. Krylov [a], Anna A. Tikhonova [a], Elena A. Ivantsova [a]

[a] Volgograd State University, Russian Federation

Abstract

This article aims to show certain features in the frequency of individual dominant and subdominants of arid phytocenoses in the composition of technogenic intrusions, directly adjacent and negatively affecting the cultural agrocenoses. To substantiate the consort relationships of these plants with other ecosystem participants, we analyzed the fragments of their proteomes with respect to key manganese- and zinc-containing proteins. As a result, the concentration of mobile forms of manganese and zinc in the soil of arid territories was shown to be a significant forming factor for the structure of dominant and subdominant technogenic intrusions in the contact zone to agrocenoses. The presence in the composition of the proteome dominants and subdominants of these vital proteins confirms the argument about the possibility of control the population size and consort activity of such plants within the phytocenosis of technogenic intrusion. The obtained data can be used to form biotechnology for optimization of agrocenoses in the conditions of the arid zone.

Keywords: arid plant communities, plant phenology, plant traits, metalloproteins, manganese, zinc, database, plant biotechnology.

1. Introduction

The arid plant communities are characterized by a constant impact of a complex of stress factors affecting significantly the metabolic re-structure of plants and microorganisms living in these areas (El-Sayed et al., 2014; He et al., 2014). Natural and anthropogenic systems directly adjacent to agrocenoses occupy a special place in this complex system of competitive relations. They create unique consort connections between soil microbiota, plants and entomofauna (Hudson et al., 2016; Liu et al., 2014). The dependence of the dynamics of metabolism and energy in such semi-artificial biocenoses on the influence of soil and climatic conditions is considered in a number of fairly extensive studies (El-Sayed et al., 2014; Mushaeva, 2015). As a result, adjacent biocenoses (intrusions) usually have an active, and more often, negative impact on the human–created ecosystem of the treated field (Ivantsova et al., 2018; Ndiribe et al., 2013).

On the other hand, interspecific connections in technogenic intrusions are not so stable. In connection with this, the attempts to change the general properties of such systems by point control actions can be effective (Drenovsky et al., 2012; Kertész et al., 2017). In particular, such effects can be found in the control of metal-containing plant proteins, the influence on which was possible both by direct molecular genetic methods, and through the regulation of metal concentration in the soil or the impact on the consort bonds in the system of metal transportation to plants (Gall et al., 2015; Ma et al., 2016).

* Corresponding author
E-mail addresses: novochadov.valeriy@volsu.ru (V.V. Novochadov)

Previously, we have shown almost complete absence of dependence between the force of technogenic intrusions influence on adjacent agricultural crops and the content of mobile forms of Nickel and copper in the soil (Ivantsova et al., 2017; Ivantsova et al., 2018). In this regard, in this study we made an attempt to consider in more detail the relationship between the presence of mobile forms of trace soil elements such as manganese and zinc, and the prevalence of individual representatives of plant communities, including in connection with the influence of intrusion on the adjacent cultivated fields.

2. Material and methods

The analysis of the concentration of mobile forms of trace elements in the soil was carried out by the precision method of atomic absorption spectrometry using the spectrometer 'Quantum.Z', LLC KORTEK, Russia (Tikhonova, 2017).

Manganese concentration in all investigated samples ranged from shaft to 510.3 of 129.5 mg/kg. In this regard, the content of trace element in the areas was assessed as low in the case, when it was less than 225 mg/kg (25 % of observations). We considered the value high in the case of Mn concentration more than 355 mg/kg (25 % of observations), the remaining cases were regarded as the average content of the mobile form of manganese in the soil. The concentration of zinc was ranked in intervals 13,3 – 23,0 – 42,6 – 52,5 mg/kg, respectively.

To study the proteome and metal-containing proteins, we selected the dominant plant species and subdominants in the studied technogenic intrusions. Bioinformatic analysis consisted in virtual screening of the database using open access resources UniProt (www.uniprot. org) and GeneOntology (http://geneontology.org). Pre-select metals were manganese or zinc. For the search we used synonymic constructs of the following type – zinc and organism: "Artemisia absinthium (Absinth wormwood) [72332]". The search included metals within the co-factor, and also atoms in metal-bond sites. Thus, we complete the selection of all metal-dependent proteins that contain metal in their structure or bind to metal for the manifestation of their activity.

The structure of the knowledge base on metal-containing proteins we built using MicrosoftExel (USA). It included the following lines: the name of the species, the names of metals, the vertical function of proteins in the body, the names of proteins, protein id in UniProt. Vertically we included data from the GeneOntology, which allow more detail to reflect the functioning of the protein. These data were found for proteins with non-annotated function is in UniProt. More significant functions of metal-containing proteins, as photosynthesis, salt tolerance, respiratory chain, etc., we selected in special column.

3. Results and discussion

Table 1 demonstrates the different types the most dominated (or were subdominants) in the plant communities of technogenic intrusions at different concentrations of the soil mobile forms of manganese and zinc.

Table 1. The dependence between the content of soil mobile forms of manganese and the frequency of domination/sub-domination of individual plants in technogenic intrusions (%)

Plant species	Concentration of soil mobile form of manganese, mg/kg		
	Low (less than 225)	Moderate (from 225 to 355)	High (more than 355)
The positive dependence on the concentration			
Artemisia lercheana *	14%	57%	57%
Atriplex tatarica *	-	36%	57%
The negative dependence on the concentration			
Cichórium íntybus	71%	21%	14%
Descurainia sophia	43%	36%	-
Lactuca tatarica *	57%	36%	14%
Tripleuros pérmuminodórum	43%	43%	-
Xanthium albinum	28%	28%	-
No dependence on the concentration			
Artemísia absínthium	57%	43%	57%

Convolvulus arvensis	28%	36%	28%
Elytrigia repens	43%	36%	43%
Euphorbia helioscopia *	28%	36%	28%
Euphorbia seguieriána *	43%	36%	43%
Crépis tectórum *	28%	50%	28%

Note: here and in the following table asterisks (*) marked the plants, other things being equal, being dominates or subdominants in intrusions with a significant negative impact on the surrounding agrocenoses.

Table 2 demonstrates the similar differences between frequency of plant dominants/subdominants according to the different concentrations of the soil mobile forms of manganese and zinc.

As you can see, there is a certain dependence for dominant plants. Some of them are more likely to dominate at relatively low concentrations of manganese or zinc, others ones prefer relatively high concentrations of trace elements in the soil. More than half of the dominants and subdominants we have no any dependence within the studied intrusions. This was partly explained by their non-permanent presence in ecosystems.

Nevertheless, it is necessary to take into account the positive dependence on the concentrations of manganese or zinc in the dominants, negatively affecting the adjacent agrocenosis. Such a finding suggests the possibility to reduce such a negative effect, selectively changing the concentration of these metals or their bioavailability with the help of agrotechnical and biotechnical measures. On the contrary, the presence of Lactuca tatarica's 'preference' for manganese allows, by increasing the concentration of ions of this metal in the soil, to reduce the impact of intrusion on agrocenosis due to the violation of the consort bonds in the community intrusion.

Table 2. The dependence between the content of soil mobile forms of zinc and the frequency of domination/sub-domination of individual plants in technogenic intrusions (%)

Plant species	Concentration of soil mobile form of zinc, mg/kg		
	Low (less than 23,0)	Moderate (from 23.0 to 42.6)	High (more than 42.6)
The positive dependence on the concentration			
Artemisia lercheana *	-	64%	57%
Atriplex tatarica *	-	43%	43%
Lactuca tatarica *	14%	43%	57%
The negative dependence on the concentration			
Artemísia absínthium	57%	57%	28%
Cichórium íntybus	57%	36%	-
Tripleuros pérmuminodórum	28%	50%	-
No dependence on the concentration			
Convolvulus arvensis	28%	36%	28%
Crépis tectórum *	43%	29%	28%
Descurainia sophia	28%	25%	28%
Elytrigia repens	28%	50%	28%
Euphorbia helioscopia *	28%	36%	28%
Euphorbia seguieriána *	43%	36%	43%
Xanthium albinum	14%	21%	28%

In the process of studying the proteomes of plants, we found, that only 6 plant species among all representatives in phytocenoses had sufficient annotations of metal-containing proteins: *Amaranthus retroflexus L., Medica gosativa L., Melilotus officinalis L. Pall., Polygonum aviculare L., Convolvulus arvensis L.,* и *Hordeum vulgare L.* (Table 3).

Table 3. Comparison of Mn- and Zn-containing proteins in proteomes of dominant/subdominant plant species in arid phytocenoses

Plant species	Metal-containing proteins			
	Annotated functions		Non-annotated functions	
	Mn	Zn	Mn	Zn
Amaranthus retroflexus	2	-	-	2
Medicago sativa	9	10	2	2
Melilotus officinalis	4	-	-	-
Polygonum aviculare	-	-	-	-
Convolvulus arvensis	2	-	-	-
Hordeum vulgare	22	90	11	107

At the same time, the proteome for the majority plants in arid zone, not included in human economic activity, has not yet been studied in detail, and the amount of annotated proteins was insignificant.

The UniProt-annotated metal-containing proteins in representatives of phytocenoses are responsible to perform functions such as photosynthesis, regulation of cell cycle and metabolism, biosynthesis of pigments, participation in the respiratory chain.

Amaranthus retroflexus L. and *Convolvulus arvensis L.* give as two manganese-containing protein each, responsible for photosynthesis, *Amaranthus retroflexus L.*, also allocated 2 protein of zinc with unknown function. We found nine annotated proteins that are associated with the manganese and is responsible for the function of photosynthesis in *Medicago sativa L.* It also had ten proteins associated with zinc, being responsible for the destruction of radicals in the cells, salt resistance, proteolytic activity, lignification, metabolism of carbon dioxide. Four manganese-containing proteins responsible for photosynthesis and separate links of the general metabolism are the annotated metalloprotein pool for the *Melilotus officinalis L. Pall.*

As a cultivated plant, *Hordeum vulgare* has 282 studied metal-dependent proteins, of which 112 were annotated with manganese (22) and zinc (90). The manganese-containing proteins are responsible for the formation of s-adenosylmethionine from methionine and ATP and participate in protective mechanisms. Zinc-containing proteins perform metabolic functions, as well as participate in ubiquitin detoxification and subsequent proteasomal degradation of target proteins (Table 4).

Table 4. The most important metal-containing proteins in the dominant plant species of arid technogenic intrusions

Protein name	Function	Representatives
Manganese-containing proteins		
Photosystem II protein (EC 1.10.3.9)	Photosynthesis	*Hordeum vulgare L.* *Amaranthus retroflexus L.* *Medicago sativa L.* *Convolvulus arvensis L.* *Melilotus officinalis L.*
Isocitrate dehydrogenase [NADP], chloroplastic (EC 1.1.1.42)	Basic metabolism	*Medicago sativa L.*
S-adenosylmethionine synthase (EC 2.5.1.6)		*Medicago sativa L.*
S-adenosylmethionine synthase (EC 2.5.1.6)		*Hordeum vulgare L.*
Serine/threonine-protein phosphatase PP2A catalytic subunit (EC 3.1.3.16)	Cell cycle regulation	*Medicago sativa L.*
Oxalateoxidase 1 (EC 1.2.3.4)	Defense mechanism	*Hordeum vulgare L.*

Zinc-containing proteins		
Carbonic anhydrase (EC 4.2.1.1)	Carbon dioxide metabolism	*Medicago sativa L.*
Acetyl-CoA carboxylase carboxyl transferase subunit beta, chloroplastic (EC 6.4.1.2)	Regulation of the basic metabolism	*Medicago sativa L.*
Glutamate--tRNA ligase, chloroplastic/mitochondrial (EC 6.1.1.17)		*Hordeum vulgare L.*
Protein arginine methyltransferase (EC 2.1.1.320)	Basic metabolism	*HordeumvulgareL.*
ATP-dependent zinc metalloprotease FTSH, chloroplastic (EC 3.4.24.-)		*Medicago sativa L.*
Methionine synthase (Fragment)		*Medicago sativa L.*
Methylthioribulose-1-phosphate dehydratase (EC 4.2.1.109)		*Hordeum vulgare L.*
E3 ubiquitin-protein ligase (EC 2.3.2.27)		*Hordeum vulgare L.*
Histidinol dehydrogenase, chloroplastic (EC 1.1.1.23)		*Hordeum vulgare L.*
Cinnamylalcoholdehydrogenase (EC 1.1.1.195)	The formation of cell wall, the scent	*Medicago sativa L.*
Pollen allergen MetE (EC 2.1.1.14)	Non-annotated	*Amaranthus retroflexus L.*

Starting the discussion, we emphasize that we have identified not absolute, but only relative preferences of dominant and subdomains of intrusive phytocenoses in the arid zone to one or another concentration of mobile forms of soil manganese. This dependence is fuzzy, because it could not be decisive in the ability of a plant to grow in the natural environment of its habitat (He et al., 2016; He et al., 2016).

Both of these elements are essential metals, but the peculiarities of their metabolism in plants of different species lead to differences in their needs and, accordingly, in different reactions to changes in their concentration in the soil (Leszczyszyn et al., 2013; Sorty et al., 2016).

As shown by the research, a lot of metal-dependent proteins, especially-containing manganese, involved in photosynthesis and energy exchange in plants. The zinc-containing proteins are involved in the performance of specific functions such as lignification, synthesis of aromatic substances of the plant, as well as maintenance of salt stability, regulation of fatty acid synthesis. Other important functions provided by the presence of metal-dependent proteins are metabolic and transport.

Naturally, only the evolutionary processes may explain all specific generic and species mechanisms of adaptation to environmental conditions, based on the processes of biochemical transformation of manganese and zinc. The basic mechanism of this process is the regulated flow of these microelements from the soil, which is largely determined by the composition and activity of the soil microbiota (Bargaz et al., 2018; Gibbons et al., 2017; Vardharajula et al., 2011).

The revealed dependences may form the basis of such biotechnological strategies, which were able to limit the number and consort influence of a number of "undesirable" plant dominants on the adjacent agricultural plant communities (Dudchenko, 2012; Gibbons et al., 2017). We believe it is possible to develop on this basis, to stimulate the number and activity of subdominants, which, according to our previous studies (Ivantsova et al., 2017; Ivantsova et al., 2018), was accompanied by increased intraspecific competition within phytocenosis and weakening its influence on contact plant communities.

4. Conclusion

The concentration of mobile forms of manganese and zinc in the soil of arid territories was shown to be a significant forming factor for the structure of dominant and subdominant

technogenic intrusions in the contact zone to agrocenoses. The presence in the composition of the proteome dominants and subdominants of these vital proteins confirms the argument about the possibility of control the population size and consort activity of such plants within the phytocenosis of technogenic intrusion. The program of impacts adapted to regional conditions in the long term is able to provide its economic accessibility for individual land users, the needs of which are focused on the technology of point regulation of the state of agrocenoses.

5. Acknowledgments

This work was supported by the Ministry of Education and Science of the Russian Federation (Project no. 40.7534.2017/BC "Development of ecologically-oriented biotechnologies for the optimization of arid agrobiocenoses in the South of Russia based on the achievements of physicchemical biology and bioinformatics".

References

Bargaz et al., 2018 – *Bargaz, A., Lyamlouli, K., Chtouki, M. et. al.* (2018). Soil microbial resources for improving fertilizers efficiency in an integrated plant nutrient management system. *Frontiers in Microbiology*. 9: 1606. DOI: 10.3389/fmicb.2018.01606

Drenovsky et al., 2012 – *Drenovsky, R.E., Grewell, B.J., D'Antonio, C.M. et al.* (2012). A functional trait perspective on plant invasion. *Annals of Botany*. 110 (1): 141–153. DOI: 10.1093/aob/mcs100

Dudchenko, 2012 – *Dudchenko, L.V.* (2012). An effective biological method of weed suppression in the field-protective forest plantations. *Dostizheniya nauki i tekhniki APK*. (7): 37-38.

El-Sayed et al., 2014 – *El-Sayed, W.S., Akhkha, A., El-Naggar, M.Y. et al.* (2014). In vitro antagonistic activity, plant growth promoting traits and phylogenetic affiliation of rhizobacteria associated with wild plants grown in arid soil. *Front. Microbiol.* 5: 651.

Gall et al., 2015 – *Gall, J.E., Boyd, R.S., Rajakaruna, N.* (2015). Transfer of heavy metals through terrestrial food webs: A review. *Environ. Monit. Assess.* 187: 201. DOI: 10.1007/s10661-015-4436-3

Gibbons et al., 2017 – *Gibbons, S.M., Lekberg, Y., Mummey, D.L. et al.* (2017). Invasive plants rapidly reshape soil properties in a grassland ecosystem. *mSystems*. 2(2): e00178-16. DOI: 10.1128/mSystems.00178-16

He et al., 2014 – *He, M.Z., Dijkstra, F.A., Zhang, K. et al.* (2014) Leaf nitrogen and phosphorus of temperate desert plants in response to climate and soil nutrient availability. *Scientific Reports*. (4): e6932. DOI: 10.1038/srep06932

He et al., 2016 – *He, M.Z., Dijkstra, F.A., Zhang, K. et al.* (2016). Influence of life form, taxonomy, climate, and soil properties on shoot and root concentrations of 11 elements in herbaceous plants in a temperate desert. *Plant and Soil*. 398 (102): 339-350. DOI: 10.1007/s11104-015-2669-0

Hudson et al., 2016 – *Hudson, L.N., Newbold, T., Contu, S. et al.* (2016) The database of the PREDICTS (Projecting Responses of Ecological Diversity in Changing Terrestrial Systems) project. *Ecol. Evol.* 7(1): 145-188. DOI: 10.1002/ece3.2579

Ivantsova et al., 2017 – *Ivantsova, E.A., Novochadov, V.V., Onistratenko, N.V., Postnova, M.V.* (2017). Ecological aspects of phytosanitary optimization of arid agrobiocenoses in South Russia. *Bulgarian J. Agric. Sci.* 23(5): 834-842.

Ivantsova et al., 2018 – *Ivantsova, E.A., Onistratenko, N.V., German, N.V. et al.* (2018). Targered changes in the natural and semi-artifical arid phytocenoses in the contact zone with the agrocenoses: a system control model-based approach. *Eur. J. Mol. Biotech.* 6 (1): 53-60. DOI: 10.13187/ejmb.2018.1.53

Kertész et al., 2017 – *Kertész, M., Aszalós, R., Lengyel, A., Ónodi, G.* (2017) Synergistic effects of the components of global change: Increased vegetation dynamics in open, forest-steppe grasslands driven by wildfires an d year-to-year precipitation differences. *PLoS One*. 12(11): e0188260. DOI: 10.1371/journal.pone.0188260

Leszczyszyn et al., 2013 – *Leszczyszyn, O.I., Imam, H.T., Blindauer, C.A.* (2013). Diversity and distribution of plant metallothioneins: A review of structure, properties and functions. *Metallomics*. 5: 1146–1169. DOI: 10.1039/c3mt00072a

Liu et al., 2014 – *Liu, H., Zhang, D., Yang, X. et al.* (2014). Seed dispersal and germination traits of 70 plant species inhabiting the Gurbantunggut desert in Northwest China. *Sci. World J.* e346405. DOI: 10.1155/2014/346405

Ma et al., 2016 – *Ma, Y., Oliveira, R.S., Freitas, H., Zhang, C.* (2016). Biochemical and molecular mechanisms of plant-microbe-metal interactions: relevance for phytoremediation. *Front. Plant Sci.* 7: e918. DOI: 10.3389/fpls.2016.00918

Meena et al., 2017 – *Meena, K.K., Sorty, A.M., Bitla, U.M. et. al.* (2017). Abiotic stress responses and microbe-mediated mitigation in plants: the omics strategies. *Front. Plant Sci.* 8: 172. DOI: 10.3389/fpls.2017.00172

Mushaeva, 2015 – *Mushaeva, K.B.* (2015). Assessment of the current state of agropastoral landscapes in semi-arid areas of the Kalmykia republic with application of GIS-technologies. *Sci. J. Volgograd St. Univ. Natural Sci.* (1), 103-110. DOI: 10.15688/jvolsu11.2015.1.11

Ndiribe et al., 2013 – *Ndiribe, C., Pellissier, L., Antonelli, S. et al.* (2013). Phylogenetic plant community structure along elevation is lineage specific. *Ecol. Evol.* 3(15): 4925-4939. DOI: 10.1093/jpe/rtt064

Sorty et al., 2016 – *Sorty, A.M., Meena, K.K., Choudhary, K. et. al.* (2016). Effect of plant growth promoting bacteria associated with halophytic weed (*Psoralea corylifolia L*) on germination and seedling growth of wheat under saline conditions. *Appl. Biochem. Biotech.* 180(5): 872-882. DOI: 10.1007/s00253-017-8550-8

Tikhonova, 2017 – *Tikhonova, A.A.* (2017). Atomic absorption spectrometry in local monitoring of heavy metals (on the example of solid sediments). *Sci. J. Volgograd St. Univ. Natural Sci.* 7(1): 34-41. DOI: 10.15688/jvolsu11.2017.1.4

Vardharajula et al., 2011 – *Vardharajula, S., Ali, S.Z., Grover, M. et. al.* (2011). Drought-tolerant plant growth promoting *Bacillus* spp.: effect on growth, osmolytes, and antioxidant status of maize under drought stress. *J. Plant Interactions.* 6(1): 1-14. DOI: 10.1007/s10725-015-0142-y

Zefferman et al., 2015 – *Zefferman, E., Stevens, J.T., Charles, G.K. et al.* (2015) Plant communities in harsh sites are less invaded: a summary of observations and proposed explanations. *AoB Plants.* 7(1): plv056. DOI: 10.1093/aobpla/plv056

Published in the Slovak Republic
European Journal of Molecular Biotechnology
Has been issued since 2013.
E-ISSN: 2409-1332
2018, 6(2): 83-95

DOI: 10.13187/ejmb.2018.2.83
www.ejournal8.com

Synthesis, Electronic Transitions and Antimicrobial Activity Evaluation of Novel Monomethine and Trimethine Cyanine Dyes

H.A. Shindy [a, *], M.A. El-Maghraby [a], M.M. Goma [a], N.A. Harb [a]

[a] Department of Chemistry, Faculty of Science, Aswan University, Aswan 81528, Egypt

Abstract

New polyheterocyclic starting material compound namely 3, 5-dimethyl-7-phenyl-furo [(3,2-d) pyrazole;(3',2'-d) oxazole] was prepared and oriented for the synthesis of novel monomethine cyanine dyes (simple cyanine dyes), bis monomethine cyanine dyes (bis simple cyanine dyes), trimethine cyanine dyes (carbocyanine dyes) and bis trimethine cyanine dyes (bis carbocyanine dyes). The electronic transitions of all the synthesized cyanine dyes were evaluated and determined through investigating their visible absorption spectra in 95 % ethanol solution. The dyes were thought to be better electronic transitions when they absorb light at higher wavelength bands (bathochromic shifted and/or red shifted dyes). Consequently, the electronic transitions of the dyes decreases when they absorb light at lower wavelength bands (hypsochromic shifted and/or blue shifted dyes). The antimicrobial activity evaluation for a number of 10 (ten) selected compounds was tested against 4 (four) various bacterial strains (Bacillus subtilis, Escherichia coli, Pseudomona aeruginosa and Staphylococcus aureus). The antimicrobial activity evaluation can be made through measuring the inhibition zone diameter of the tested compounds against a number of bacterial and/or fungi strains. The compounds were thought to be better antimicrobial active when they give higher inhibition zone diameter against the tested bacterial and/or the fungi strains. Consequently, the antimicrobial activity of the compounds decrease when they give lower inhibition zone diameter against the tested bacterial and/or the fungi strains. Structural characterization and determination was carried out via elemental analysis, visible, mass, IR and ^{1}HNMR spectroscopic data.

Keywords: cyanine dyes, methine cyanine dyes, synthesis, electronic transitions, antimicrobial activity.

1. Introduction

Cyanine dyes (Shindy, 2012; Shindy, 2016; Shindy, 2017; Shindy, 2018) are important class of functional dyes and possesses an excellent photochemical and photophysical properties, such as high molar extinction coefficients (molar absorptivity), tunable fluorescence intensities, narrow absorption bands, moderate quantum yields and absorb light mainly in the visible region, but also include (cover) UV and NIR regions (larger than any other class of dye system). Therefore, an extensive number of cyanine dyes have been synthesized and developed for numerous applications in photographic processes and more recently as fluorescent probes for bio-molecular labeling and imaging (Mishra et al., 2000; Pisoni et al., 2014; Wada et al., 2015; Hyun et al., 2014; Hyun et al., 2015; Njiojob et al., 2015; Hyun et al., 2015; El-Shishtawy et al., 2010; Henary, Levitz, 2013). On the other side, pyrazole derivatives have great interest in agrochemical, pharmaceutical,

* Corresponding author
E-mail addresses: hashindy2@hotmail.com (H.A. Shindy)

and chemical industries (Keter, Darkwa, 2012; Fustero et al., 2011). In addition, pyrazole derivatives possess a wide range of bioactivities (Fustero et al., 2011; Ouyang et al., 2008), including anti-inflammatory (Gokhan-Kelekci et al., 2007), anticonvulsant (Kaushik et al., 2010), anticancer (Balbia et al., 2011), and antifungal (Vicentini, 2007) behavior. Besides, Oxazole compounds play a fundamental role in the synthesis of numerous biologically active drugs such as analgesics, antiinflammatory, antimicrobial, anticancer, antidepressants, antidiabetic and antiobesity. Spirocyclopropyl oxazolones is the novel class of inhibitor of herpes protease. Phenacyl oxazolone involves the intermolecular Diels-Alder reaction, ensuing in synthesis of anti-cancer drugs, pancratistantin and a phenanthrene alkaloid (Sweta et al., 2017; Turchi, 1986). Based on this concepts, In this research paper we prepared new pyrazolo/oxazole cyanine dyes as new synthesis contribution, spectroscopic investigation and antimicrobial evaluation in the field and with the hope that a combination of the favourable properties of both pyrazole, oxazole and cyanine dyes may be achieved.

2. Results and discussion

2.1. Synthesis

An equimolar ratios of 4-bromo-3-methyl-1-phenyl-5-pyrazolone (1) and 2-methyl-oxazole-5-one (2) were reacted in pyridine and achieved 3, 5-dimethyl-7-phenyl-furo[(3,2-d)pyrazole; (3',2'-d) oxazole] (3) as new polyheterocyclic starting material compound, Scheme (1).

Quaternization of (3) using an excess of iodoethane led to the formation of 4,6-diethyl-3,5-dimethyl-7-phenyl-furo[(3,2-d) pyrazolium;(3',2'-d)oxazolium] diiodide quaternary salt compound (4), Scheme (1), Table 1.

Reaction of the quaternary salt compound (4) with an iodoethane quaternary salts of either pyridine, quinoline or isoquinoline in equimolar ratios and in ethanol containing few drops of piperidine gave the 4,6-diethyl-5-methyl-7-phenyl-furo[(3,2-d)pyra- zolium; (3', 2'-d)oxazole]-3[4(1)]-monomethine cyanine dyes (5a-c), Scheme (1), Table 1.

Reaction of unimolar ratios of compound (4) with bimolar ratios of iodoethane quaternary salts of pyridine, quinoline or isoquinoline in ethanol containing piperidine yielded the 4,6-diethyl-7-phenyl-furo[(3,2-d)pyrazole;(3',2'-d)oxazole]-3,5[4(1)]-bis monomethine cyanine dyes (6a-c), Route (1), Scheme (1), Table 1.

Chemical confirmations for compounds (6a-c) took place via reactions of the previously prepared monomethine cyanine dyes (5a-c) with equimolar ratios of iodoethane quaternary salts of either pyridine, quinoline or isoquinoline in ethanol catalyzed by piperidine through Route (2) to achieve the same bis monomethine cyanine dyes (6a-c) obtained through route 1, characterized by melting points, mixed melting points, same visible, IR and ^{1}H-NMR spectral data, Scheme (1), Route (2), Table 1.

Reaction of the bis quaternized compound (4) with a bimolar ratios of triethylorthoformate in ethanol containing piperidine and led to the formation of the intermediate compound 4,6-diethyl-7-phenyl-furo[(3,2-d) pyrazolium; (3',2'-d) oxazolium]-3,5-bis(1,1'-diethoxy)ethyl-diiodide quaternary salt (7), Scheme (1), Table 2.

This intermediate compound (7) was then reacted with equimolar or bimolar ratios of N-ethyl (2-picolinium, quinaldinium, 4-picolinium) iodide quaternary salts in ethanol containing piperidine as a basic catalyst to give the 4,6-diethyl-5(1,1'-diethoxy)ethyl-7-phenyl-furo[(3,2-d)pyrazolium;(3',2'-d)oxazole]-3[2(4)]-trimethine cyanine dyes (8a-c) or 4,6-diethyl-7-phenyl-furo[(3,2-d) pyrazole;(3',2'-d)oxazole]-3,5[2(4)]-bis trimethine cyanine dyes (9a-c) through, Route (1), Scheme (1), Table 2, respectively.

Chemical confirmations for the bis trimethine cyanine dyes (9a-c) took place through the reaction of the previously prepared trimethine cyanine dyes (8a-c) with equimolar ratios of N-ethyl (2-picolinium, quinaldinium, 4-picolinium) iodide quaternary salts in ethanol catalyzed by piperidine through, Route (2), to achieve the same bis trimethine cyanine dyes (9a-c) obtained through Route (1), characterized by the same melting points, mixed melting points, the same visible, IR and ^{1}H-NMR spectra, Scheme (1), Route (2), Table 2.

The structure of the prepared compound was characterized and identified by elemental analysis Tables 1 and 2, visible spectra Tables 1 and 2, Mass spectrometer, IR (Wade, 1999) and ^{1}H-NMR (Wade, 1999a) spectroscopic data, Table 3.

2.2. Electronic transitions evaluation

Visible electronic transitions for all the synthesized cyanine dyes was determined through investigating their electronic visible absorption spectra in 95 % ethanol solution. The dyes were thought to be better electronic transitions when they absorb light at higher wavelength bands (bathochromic shifted and/or red shifted dyes). Consequently, the electronic transitions of the dyes decreases when they absorb light at lower wavelength bands (hypsochromic shifted and/or blue shifted dyes). So, we may say that the electronic transitions of one dye is higher than the other one if the wavelength of the maximum absorption spectrum of the former one is longer than that of the latter one. In contrary, we may say that the electronic transitions of one dye is lower than the other one if the wavelength of the maximum absorption spectrum of the former one is shorter than that of the latter one (Shindy, 2018).

The visible electronic transitions absorption spectra of the monomethine cyanine dyes (5a-c) and the bis monomethine cyanine dyes (6a-c) in 95 % ethanol solution discloses bands in the visible region 385-540 nm and 390-550 nm, respectively. The positions of these bands and their molar extinction coefficient (molar absorptivity) are largely influenced by the nature of the heterocyclic quaternary residue (A), their linkage positions and by the number of the electronic charge transfer pathways inside the dyes molecules.

So, substituting A=1-ethyl pyridinium-4-yl salts in the monomethine cyanine dye 5a and in the bis monomethine cyanine dye 6a by A=1-ethyl quinolinium-4-yl salts to get the monomethine cyanine dye 5b and the bis monomethine cyanine dye 6b causes strong bathochromic shifts by 20 nm, accompanied by increasing the number and intensity of the absorption bands in the case of the bis monomethine cyanine dye 6b, Scheme (1), Table 1. This can be attributed to increasing π-delocalization conjugation in the latter dyes due to the presence of quinoline ring system in correspondance to the pyridine ring system in the former dyes.

Changing the linkage positions from 1-ethyl quinolinium-4-yl salts to 2-ethyl isoquinolinium-1-yl salts passing from the monomethine cyanine dye 5b and the bis monomethine cyanine dye 6b to the monomethine cyanine dye 5c and the bis monomethine cyanine dye 6c resulted in a remarkable blue shifts by 10 nm accompanied by decreasing the number and intensity of the absorption bands, Scheme (1), Table 1. This can be explained in the light of decreasing the length of the π-delocalization conjugation in the latter 2-ethyl isoquinolinium-1-yl salts dyes 5c and 6c compared to the former 1-ethyl quinolinium-4-yl salts dyes 5b and 6b.

Comparing the electronic visible absorption spectra of monomethine cyanine dyes (5a-c) with those of the bis monomethine cyanine dyes (6a-c) declared that the latter dyes have bathochromically shifted bands related to the former ones. This can be attributed to the presence of two factors. The first factor is the presence of two electronic charge transfer pathways inside the latter dyes molecules in correspondance to one electronic charge transfer pathways inside the former dyes molecules, Scheme (2). The second factor is increasing conjugation due to increasing the number of methine units in bis monomethine cyanine dyes (6a-c) related to the former monomethine cyanine dyes (5a-c) by one methine unit. Scheme (1), Table 1.

Additionally, the visible electronic transitions absorption spectra of the trimethine cyanine dyes (8a-c) and the bis trimethine cyanine dyes (9a-c) in 95 % ethanol solution discloses bands in the visible region 440-650 nm and 440-660 nm, respectively. The positions of these bands and their molar extinction coefficient are largely influenced by the nature of the heterocyclic quaternary residue (A), their linkage positions and by the number of the electronic charge transfer pathways inside the dyes molecules.

So, substituting A=1-ethyl pyridinium-2-yl salts in the trimethine cyanine dye 8a and in the bis trimethine cyanine dye 9a by A=1-ethyl quinolinium-2-yl salts to get the trimethine cyanine dye 8b and the bis trimethine cyanine dye 9b causes strong bathochromic shifts by 20 nm, accompanied by increasing the number and intensity of the absorption bands in the case of the bis trimethine cyanine dyes 9b, Scheme (1), Table 2. This can be attributed to increasing π-delocalization conjugation in the latter dyes due to the presence of quinaldinium structure system ring system in correspondance to the presence of α-picolinium structure system in the former dyes.

Changing the linkage positions from 2-yl salts to 4-yl salts passing from the trimethine cyanine dye 8a and the bis trimethine cyanine dye 9a to the trimethine cyanine dye 8c and the bis trimethine cyanine dye 9c resulted in a remarkable red shifts by 10 nm accompanied by increasing the number and intensity of the absorption bands, Scheme (1), Table 2. This can be explained in

the light of increasing the length of the π-delocalization conjugation in the latter 4-yl salts dyes 8c and 9c due to the presence of the γ-picolinium structure system compared to the former 2-yl salts dyes 8a and 9a which contain the α-picolinium structure system.

Comparing the visible electronic transitions absorption spectra of trimethine cyanine dyes (8a-c) with those of the bis trimethine cyanine dyes (9a-c) declared that the latter dyes have bathochromically shifted bands related to the former ones. This can be attributed to the presence of two factors. The first factor is related to the presence of two electronic charge transfer pathways inside the latter dyes molecules in correspondance to one electronic charge transfer pathways inside the former dyes molecules, Scheme (2). The second factor is attributed to increasing conjugation due to increasing the number of methine groups in the later dyes than that of the former dyes by three methine units, Scheme (1), Table 2.

Comparison the electronic visible absorption spectra of the monomethine cyanine dye (5a-c) with those of the trimethine cyanine dyes (8a-c) reveals that the later dyes have bathochromic shifted and intensified bands than that of the former dyes. This can be related to increasing conjugation due to increasing the number of methine groups between the basic center (nitrogen atom) and the acidic center (quaternary salt) in latter dyes by two methine units, Scheme (1), Tables 1 and 2.

Comparison the electronic visible absorption spectra of the bis trimethine cyanine dyes (9a-c) with those of the bis monomethine cyanine dyes (6a-c) showed that the fomer bis trimethine cyanine dyes (9a-c) have red shifted and intensified absorption bands in comparison to the latter bis monomethine cyanine dyes (6a-c), Tables 1 and 2. This can be attributed to increasing conjugation due to increasing the number of methine units in the former bis trimethine cyanine dyes (9a-c) by four methine units, Scheme (1), Tables 1 and 2.

2.3. Antimicrobial activity evaluation

Antimicrobial activity evaluation of cyanine dyes can be made through measuring their inhibition zone diameter against a number of bacterial and/or fungi strains. The cyanine dyes were thought to be better antimicrobial active when they give higher inhibition zone diameter against the tested bacterial and/or the fungi strains. Consequently, the antimicrobial activity of the cyanine dyes decrease when they give lower inhibition zone diameter against the tested bacterial and/or the fungi strains. So, we may say that the antimicrobial activity of one cyanine dye is stronger than the other one if the inhibition zone diameter against the tested bacterial and/or the fungi strains of the former one is higher than that of the latter one. In contrary, we may say that the antimicrobial activity of one cyanine dye is weaker than the other one if the inhibition zone diameter against the tested bacterial and/or the fungi strains of the former one is lower than that of the latter one.

Studying the antimicrobial activity evaluation against a number of bacterial and/or fungi strains bears to have a great practical value and very important in the case of cyanine dyes because the extensive uses and applications of these dyes as bactericidal (anti-bacterial strains) and/or as fungicidal (anti-fungi strains) in pharmaceutical (pharmacological) industry and/or in pharmacochemistry.

So, in this study, the antimicrobial activity evaluation for a number of 10 (ten) selected newly synthesized compounds (3, 4, 5b, 6a, 6b, 6c, 7, 9a, 9b, 9c) were studied and determined against a number of 4 (four) bacterial strains (Bacillus subtilis, Escherichia coli, Pseudomonas aeruginosa, Staphylococcus aureus), Table 4. According to this study, it was observed that:

Comparing the antimicrobial activity of compound (3) and its iodoethane quaternary salt (4), showed that, the latter compound (4) have higher effect to destroy the bacterial strains Table (4). This may be related to increasing the electron attracting character of compound (4) due to quaternization, Scheme (1).

The bacterial inhibition effects of the compounds (3) and (4) have a remarkable decrease if compared by their derived bis monomethine cyanine dyes (6a-c), Table 4. This could be related to the cyanine dyes structure effects in these compounds, Scheme (1).

Comparison between the antimicrobial activity of the bis monomethine cyanine dyes (6a-c) and the bis trimethine cyanine dyes (9a-c) showed that, the latter dyes possess lower potency as antimicrobial activity than the former ones Table 4. This might be correlated to increasing number of methine groups in the latter dyes (9a-c) by four methine units, Scheme (1).

Changing the quaternary salts in the bis monomethine cyanine dyes (6a-c) from 1-ethyl pyridinnium-4-yl salt in dye (6a) to 1-ethyl quinolinium-4-yl salt and/or 2-ethyl isoquinolinium-1-

yl salt to get dyes (6b) and / or (6c), discloses that the latter dyes have lower antimicrobial effects on the bacterial strains, Table 4. This might be attributed to increasing π-delocallization conjugation in the latter dyes (6b), (6c) due to the presence of quinoline and / or isoquinoline ring system in correspondance to pyridine ring system in the former dye (6a), Scheme (1).

Changing the type of the quaternary heterocyclic residue and / or their linkage position in the bis trimethine cyanine dyes (9a-c) from 1-ethyl pyridinium-2-yl salt in dye (9a) to 1-ethyl quinolinium-2-yl salt and/or 1-ethyl pyridinium-4-yl salt to obtain dyes (9b) and / or (9c) declared that the former dye (9a) have higher antimicrobial activity for all the bacterial strains, Table (4). This could be related to increasing π-delocalization conjugation in the latter dyes (9b) and / or (9c) due to the presence of quinaldinium and / or γ-picolinium nucleus in correspondance to α-picolinium nucleus in the former dye (9a), Scheme (1).

Comparison the antibacterial activity of the monomethine cyanine dye (5b) with the bis monomethine cyanine dye (6b) showed that the latter one have higher inhibition zone diameter against Staphylococcus aureus and Escherichia coli bacterial strains, Table (4). This reflects its increased ability to may be used and / or applied as antimicrobial active compound against these two bacterial strains. This effect may be attributed to increasing either of the number of methine units in the bis monomethine cyanine dye (6b) by one methine unit compared with the monomethine cyanine dye (5b), Scheme (1) and / or increasing the number of the electronic charge transfer pathways inside the dye (6b) which contain two electronic charge transfer pathways compared with dye (5b) which contain one electronic charge transfer pathways in its structure, Scheme (2).

Comparing the antimicrobial activity of the bis monomethine cyanine dye (6b) with their analogous (6c) declared that the latter dye (6c) possesses higher potency effect against all the bacterial strains, Table (4). This may be related to the presence of the isoquinoline nucleus in the latter dye (6c) in correspondance to quinoline nucleus in the former dye (6b), Scheme (1).

The antimicrobial activity of the bis trimethine cyanine dye (9b) showed higher inhibition zome diameter against Staphylococcus aureus compaired with their analogous bis trimethine cyanine dye (9c) Table (4). This reflect its increased ability to may be used and / or applied as antimicrobial active against this bacterial strain. This effect may be related to the presence of quinaldinium ring system in dye (9b) compared to γ-picolinium ring system in dye (9c), Scheme (1).

General comparison the antimicrobial activity of the bis trimethine cyanine dyes (9a-c) declared that these dyes possesses higher potency effect against the Escherichia coli and Pseudomonas aeruginosa bacterial strains compared with Bacillus subtilis and Staphylococcus aureus bacterial strains, Table 4. This reflects their increased activity to may be used and / or applied as antimicrobial active compounds against the former bacterial strains.

Comparison the antimicrobial activity of the compounds (3) and / or (4) with their derived bis trimethine cyanine dyes (9a-c) displayed that the latter dyes compounds (9a-c) have higher potency effects for most of the bacterial strains, Table 4. This could be attributed to the cyanine dyes structure effects in the latter dyes (9a-c), Scheme (1).

Substituting the 3 and 5 di methyl groups in compound (4) by 3 and 5 di $CH_2CH(OEt)_2$ groups to get compound (7) make decreasing for the inhibition effects for all the bacterial strains, Table 4. This could be attributed to the strong electron pulling character of the diethoxy group in compound (7) in correspondance to the electron pushing character of CH_3 in compound (4), Scheme (1).

Converting the intermediate compounds (7) to its derived bis trimethine cyanine dyes (9a-c) makes increasing for the antimicrobial inhibition zone diameter for all the bacterial strains, Table (4). This could be related to the cyanine dyes structure effects in these compounds, Scheme (1).

General comparison of the antimicrobial activity for all the tested compounds disclosed that, the bis monomethine cyanine dyes (6a) gives the highest inhibition zone diameter against all the bacterial strains, Table 4. This reflect its strong and increased effect to may used and/or applied as antimicrobial active against these bacterial strains.

General comparison of the antimicrobial activity for all the tested compounds revealed that, the intermediate compound (7) gives the lowest inhibition zone diameter against all the bacterial strains, Table 4. This indicate its negative (zero) effects and/or its non availability to may used and/or applied as antimicrobial active against these bacterial strains.

3. Conclusion

From the above discussed results we could conclude that:

1. The electronic visible absorption spectra of the monomethine (5a-c), bis monomethine (6a-c), trimethine (8a-c) and bis trimethine (9a-c) cyanine dyes in 95 % ethanol solution underwent displacements to give bathochromic and/or hypsochromic shifted bands depending upon the following factors:

A) The nature of the heterocyclic quaternary salt residue in the order of:

i) Quinolinium dyes > pyridinium dyes (in the monomethine and bis monomethine cyanine dyes).

ii) Quinaldinium dyes > α-picolinium dyes (in the trimethine and bis trimethine cyanine dyes).

B) Linkage position of the heterocyclic quaternary salt residue in the order of:

i) quinolinium dyes > isoquinolinium dyes (in the monomethine and bis monomethine cyanine dyes).

ii) γ-picolinium dyes > α-picolinium dyes (in the trimethine and bis trimethine cyanine dyes).

C) The number of the methine units and / or groups between the two heterocyclic ring system of the cyanine dyes molecules in the order of:

i) trimethine cyanine dyes > monomethine cyanine dyes.

ii) bis trimethine cyanine dyes > bis monomethine cyanine dyes.

D) The number of the electronic charge transfer pathways inside the dyes molecules in the order of: two electronic charge transfer pathways dyes > one electronic charge transfer pathways dyes (bis monomethine cyanine dyes > monomethine cyanine dyes; bis trimethine cyanine dyes > trimethine cyanine dyes).

2. The intensity of the colours of the monomethine cyanine dyes, bis monomethine cyanine dyes, trimethine cyanine dyes and bis trimethine cyanine dyes are illustrated according to the following suggested two mesomeric electronic transitions structures (A) and (B) producing a delocalized positive charges over the conjugated chromophoric group system of the dyes, Scheme (2).

3. The antimicrobial inhibition action activity of the synthesized compounds (3, 4, 5b, 6a, 6b, 6c, 7, 9a, 9b, 9c) increase and/or decrease to give higher and/or lower bacterial inhibition zone diameter depending upon the following factors:

a – Types of cyanine dyes molecules (monomethine, bis monomethine, bis trimethine cyanine dyes).

b – Nature of the heterocyclic quaternary salt residue (A). (pyridinium and/or quinolininium salt residue; α-picolinium and/or quinaldinium salt residue).

c – Linkage positions of the heterocyclic quaternary salt residue (A) (quinolinium and/or isoquinolinium salt residue; α-picolinium and/or γ-picolinium salt residue).

f – Kind of the bacterial strains: higher in the case Escherichia coli and Pseudomonas aeruginosa bacterial strains and lower in the case Bacillus subtilis and Staphylococcus aureus bacterial strains (in the case of the bis trimethine cyanine dyes 9a-c).

4. Experimental

4.1. General

All the melting points of the prepared compounds are measured using Electrothermal 15V, 45W 1 A9100 melting point apparatus, Chemistry department, Faculty of Science (Aswan University) and are uncorrected. Elemental analysis was carried out at the Microanalytical Center of Cairo University by an automatic analyzer (Vario EL III Germany). Infrared spectra were measured with a FT/IR (4100 Jasco Japan), Cairo University. ^{1}H NMR Spectra were accomplished using Varian Gemini-300 MHz NMR Spectrometer (Cairo University). Mass Spectroscopy was recorded on Mas 1: GC-2010 Shimadzu Spectrometer (Cairo University). Electronic visible absorption spectra were carried out on Visible Spectrophotometer, Spectro 24 RS Labomed, INC, Chemistry department, Faculty of Science (Aswan University). Antimicrobial activity screening were carried out at the Microanalytical center, Microbiology division (Cairo University).

4.2. Synthesis

4.2-1. Synthesis of 3, 5-dimethyl-7-phenyl-furo[(3,2-d)pyrazole;(3',2'-d)oxazole] (3)

Equimolar ratios of 4-bromo-3-methyl-1-phenyl-5-pyrazolone (1) (0.01 mol, 2.5 gm) and 2-methyl-oxazole-5-one (2) (0.01 mol, 1 gm) were dissolved in pyridine (50 ml). The reaction mixture was heated under reflux for (6-8 hrs) until the mixture attained brown colour. It was filtered off while hot to remove any impurities, concentrated, then poured in ice water mixture with continuous shaking. The precipitated compound was filtered, washed with cold water, air dried, collected and crystallized from ethanol. The data are reported in Table 1.

4.2-2. Synthesis of 4,6-diethyl-3,5-dimethyl-7-phenyl-furo[(3,2-d)pyrazolium; (3',2'-d)oxazolium]diiodide quaternary salt (4)

Apure crystallized sample of (3) (0.04 mol, 1.2 gm) was suspended in excess of iodoethane (30 ml) and heated gently under reflux at low temperature (40-60°C) for 1hr. The solvent was evaporated and the residue was collected and crystallized from ethanol. See data in Table 1.

4.2-3. Synthesis of 4,6-diethyl-5-methyl-7-phenyl-furo[(3,2-d)pyrazolium;(3',2'-d)oxazole]-3[4(1)]-monomethine cyanine dyes (5a-c)

A mixture of compound (4) (0.01 mol, 0.8 gm) and iodoethane quaternary salts (0.01 mol) of pyridine (0.35 gm), quinoline (0.4 gm), or isoquinoline (0.4 gm) was refluxed in ethanol (50 ml) containing piperidine (3-5 drops) for 6-8 hrs. The reaction mixture, which changed from brown to red during the refluxing time, was filtered off while hot to remove any impurities, concentrated, cooled and precipitated by adding cold water. The precipitated products were collected and crystallized from ethanol. The relevant data are given in Table 1.

4.2-4. Synthesis of 4,6-diethyl-7-phenyl-furo[(3,2-d)pyrazole;(3',2'-d)oxazole]-3,5[4(1)]-bis monomethine cyanine dyes (6a-c)

Two different routes are employed to prepare these cyanine dyes:

Route (1): Piperidine (3-5 drops) was added to an ethanolic solution (50 ml) of (4) (0.01 mol, 0.8 gm) and iodoethane quaternary salts (0.02 mol) of pyridine (0.7 gm), quinoline (0.8 gm), isoquinoline (0.8 gm). The mixture was heated under reflux for 6-8 hrs, where its colour changed from brown to red during the refluxing time. It was filtered off while hot, concentrated to half its volume and cooled. The precipitated dyes were filtered, washed with water, air dried and crystallized from ethanol. The data are given in Table 1.

Route (2): The previously prepared monomethine cyanine dyes (5a-c) (0.01 mol, 0.7 gm for 5a, 0.7 gm for 5b, 0.7 gm for 5c) and iodoethane quaternary salts (0.01 mol) of pyridine (0.2 gm), quinoline (0.3 gm), isoquinoline (0.3 gm) were dissolved in ethanol (50 ml), to which piperidine (3-5 drops) was added. The reaction mixture was heated under reflux for 3-5 hrs and attained reddish brown colours at the end of the refluxing time. It was filtered off while hot, concentrated to half its volume and cooled. The precipitated dyes were filtered, washed with water, dried and crystallized from ethanol to give the same dyes obtained by route (1), characterized by melting points, mixed melting points, same visible, IR and ^{1}H-NMR spectral data, Table 1.

4.2-5. Synthesis of 4,6-diethyl-7-phenyl-furo[(3,2-d)pyrazolium; (3',2'-d)oxazolium]-3,5-bis(1,1'-diethoxy)ethyl-diiodide quaternary salt (7) as intermediate compound

This intermediate compound (7) was synthesized by refluxing of the quaternary salt compound (4) (0.04 mol, 2.4 gm) with triethylorthoformate (0.08 mol, 1.6 ml) in ethanol (50 ml) and presence of piperidine (3-5 drops) for 3-5 hrs. The dark brown mixture was filtered on hot to remove any impurities, concentrated and precipitated by cold water. The separated intermediate compound was filtered, washed with water and crystallized from ethanol. The results are registered in Table 2.

4.2-6. Synthesis of 4,6-diethyl-5(1,1'-diethoxy)ethyl-7-phenyl-furo[(3,2-d)pyrazolium; (3',2'-d)oxazole]-3[2(4)]-trimethine cyanine dyes (8a-c):

A mixture of the intermediate compounds (7) (0.01 mol, 0.8 gm) and N-ethyl α-picolinium iodide quaternary salt (0.01 mol, 0.25 gm), N-ethyl quinaldinium iodide quaternary salt (0.01 mol, 0.3 gm) or N-ethyl γ-picolinium iodide quaternary salt (0.01 mol, 0.25 gm) were heated under reflux in ethanol (50 ml) containing piperidine (3-5 drops) for 6-8 hrs. The colour of the reaction mixture attained red (for 8a), violet (for 8b) and deep red (for 8c) at the end of the refluxing time. It was filtered off on hot, concentrated and precipitated by adding cold water. The separated

cyanines were filtered, washed with cold water and crystallized from ethanol. The results are listed in Table 2.

4.2-7. Synthesis of 4,6-diethyl-7-phenyl-furo[(3,2-d) pyrazole;(3',2'-d)oxazole]-3,5[2(4)]-bis trimethine cyanine dyes (9a-c)

Two different routes are employed to prepare these cyanine dyes:

Route (1): was carried out by adding piperidine (3-5 drops) to a mixture of an ethanolic solution (50 ml) of the intermediate compound (7) (0.01 mol, 0.8 gm) and N-ethyl α-picolinium iodide quaternary salt (0.02 mol, 0.5 gm), N-ethyl quinaldinium iodide quaternary salt (0.02 mol, 0.6 gm) or N-ethyl γ-picolinium iodide quaternary salt (0.02 mol, 0.5 gm). The reaction mixture was heated under reflux for 6-8 hrs. The colour of the reaction mixture attained deep red (for 9a), deep violet (for 9b) and deep red (for 9c) at the end of the refluxing time. It was filtered off while hot, concentrated and precipitated by adding cold water. The separated cyanines were filtered, washed with cold water, air dried and crystallized from ethanol. The results are listed in Table 2.

Route (2): was accomplished through the reaction between equimolar ratios of the previously prepared trimethine cyanine dyes (8a-c) (0.01 mol) (8a, 0.8 gm), (8b, 0.9 gm), (8c, 0.8gm) and iodoethane quaternary salts (0.01 mol) of α-picoline (0.25 gm), quinaldine (0.03 gm) and γ-picoline (0.25 gm) in ethanol (50 ml) and presence of piperidine (3-5 drops). The reacting materials were refluxed for 6-8 hrs, wherever, it attained a reddish brown with α-picoline and γ-picoline and deep violet colour with quinaldine at the end of the reflux. They were filtered, while hot, concentrated, cooled and precipitated by adding cold water. The precipitates were collected and crystallized from ethanol to give the same dyes obtained by route (1), characterized by melting points, mixed melting points, same visible, IR and ^{1}H-NMR spectral data, Table 2.

4.3. Spectral Behavior

The electronic visible absorption spectra of the prepared cyanine dyes were examined in 95 % ethanol solution and recorded using 1Cm Qz cell in visible spectrophotometer 24 RS Labomed, INC. A stock solution ($1x10^{-3}$M) of the dyes was prepared and diluted to a suitable volume in order to obtain the desired lower concentrations. The spectra were recorded immediately to eliminate as much as possible the effect of time.

4.4. Antimicrobial Activity evaluation

The tested compounds (3, 4, 5b, 6a, 6b, 6c, 7, 9a, 9b, 9c) were dissolved in DMSO to give a final concentration (1 mgm/ml). Susceptible sterile discs were impregnated by the tested substance (50 µgm/disc) via a means of micropipette. The biological activity for each substance was tested on surface seeded nutrient agar medium with the prepared susceptible discs. Bacterial strains and the antimicrobial effect are shown in Table 4.

5. Conflict of interest

There is no conflict of interest.

6. Acknowledgements

We are thankful to the Chemistry department, Faculty of Science, Aswan University, Aswan, Egypt for supporting this work.

References

Balbia et al., 2011 – *Balbia, A., Anzaldi, M., Macciò, C., Aiello, C., Mazzei, M., Gangemi, R., Castagnola, P., Miele, M., Rosano, C., Viale, M.* (2011). *Eur. J. Med. Chem.*, 46, 5293-5309.

El-Shishtawy et al., 2010 – *El-Shishtawy, R.M., Asiri, A.M., Basaif, S.A., Rashad Sobahi, T.* (2010). Synthesis of a new beta-naphthothiazole monomethine cyanine dye for the detection of DNA in aqueous solution. *Spectrochim. Acta A,* 75, 1605–1609.

Fustero et al., 2011 – *Fustero, S., Sanchez-Rosello, M., Barrio, P., Simon-Fuentes, A.* (2011). *Chem. Rev.,* 111, 6984-7034.

Gokhan-Kelekci et al., 2007 – *Gokhan-Kelekci, N., Yabanoglu, S., Kupeli, E., Salgin, U., Ozgen, O., Ucar, G., Yesilada, E., Kendi, E., Yesilada, A., Bilgin, A.A. Bioorg. Med. Chem.*, 15, 5775-5786.

Henary, Levitz, 2013 – *Henary, M., Levitz, A.* (2013). Synthesis and applications of unsymmetrical carbocyanine dyes. *Dyes Pigment.,* 99, 1107–1116.

Hyun et al., 2014 – *Hyun, H., Wada, H., Bao, K., Gravier, J., Yadav, Y., Laramie, M., Henary, M., Frangioni, J.V., Choi, H.S.* (2014). Phosphonated Near-Infrared Fluorophores for Biomedical Imaging of Bone. Angew. Chem. Int. Ed. Engl. 53, 10668–10672.

Hyun et al., 2015 – *Hyun, H., Park, M.H., Owens, E.A., Wada, H., Henary, M., Handgraaf, H.J.M., Vahrmeijer, A.L., Frangioni, J.V., Choi, H.S.* (2015). Structure-inherent targeting of near-infrared fluorophores for parathyroid and thyroid gland imaging. *Nat. Med.,* 21, 192–197.

Hyun et al., 2015 –Hyun, H., Owens, E.A., Wada, H., Levitz, A., Park, G., Park, M.H., Frangioni, J.V., Henary, M., Choi, H.S. (2015). Cartilage-Specific Near-Infrared Fluorophores for Biomedical Imaging. *Angew. Chem. Int. Ed. Engl.*, 54, 8648–8652.

Kaushik et al., 2010 – *Kaushik, D., Khan, S.A., Chawla, G., Kumar, S.N.* (2010). *Eur. J. Med. Chem.*, 45, 3943-3949.

Keter, Darkwa, 2012 – *Keter, K.F., Darkwa, J.* (2012). Biometals, 25, 9-21.

Mishra et al., 2000 – *Mishra, A., Behera, R.K., Behera, P.K., Mishra, B.K., Behera, G.B.* (2000). Cyanines during the 1990s: A Review. *Chem. Rev.*, 100, 1973–2012.

Njiojob et al., 2015 - *Njiojob, C.N., Owens, E.A., Narayana, L., Hyun, H., Choi, H.S., Henary, M.* (2015). Tailored Near-Infrared Contrast Agents for Image Guided Surgery. *J. Med. Chem.,* 58, 2845–2854.

Ouyang et al., 2008 – *Ouyang, G., Cai, X.-J., Chen, Z., Song, B.-A., Bhadury, P.S., Yang, S., Jin, L.-H., Xue, W., Hu, D.-Y., Zeng, S.J.* (2008). *Agric. Food Chem.,* 56, 10160-10167.

Pisoni et al., 2014 – *Pisoni, D.S., Todeschini, L., Borges, A.C.A., Petzhold, C.L., Rodembusch, F.S., Campo, L.F.* (2014). Symmetrical and Asymmetrical Cyanine Dyes. Synthesis, Spectral Properties, and BSA Association Study. *J. Org. Chem.* 79, 5511–5520.

Shindy, 2012 – *Shindy, H.A.* (2012). Basics, Mechanisms and Properties in the Chemistry of Cyanine Dyes: A Review Paper. *Mini-Reviews in Organic Chemistry,* Volume 9, No. 4, pp. 352-360.

Shindy, 2016 – *Shindy, H.A.* (2016). Characterization, Mechanisms and Applications in the Chemistry of Cyanine Dyes: A Review. *European Journal of Molecular Biotechnology,* 14 (4), 158-170.

Shindy, 2017 –*Shindy, H.A.* (2017). Fundamentals in the Chemistry of Cyanine Dyes: A Review Dyes and Pigments, 145, 505-513.

Shindy, 2018 – *Shindy, H.A.* (2018). Novel polyheterocyclic cyanine dyes: synthesis, photosensitiztion and solvent/electronic transitions correlation. *European Reviews of Chemical Research,* 5(1), 30-39.

Shindy, 2018 – *Shindy, H.A.* (2018). Structure and solvent effects on the electronic transitions of some novel furo/pyrazole cyanine dyes. *Dyes and Pigments,* 149, 783-788.

Sweta et al., 2017 – *Sweta Joshi, Ajay Singh Bisht, Divya Juyal* (2017). Systematic scientific study of 1, 3-oxazole derivatives as a useful lead for pharmaceuticals: A review. *The Pharma Innovation Journal,* 6(1): 109-117.

Turchi, 1986 – *Turchi, I.J.* (1986). Review on Oxazoles. John Wiley and Sons, 18-20, 0331-10338.

Vicentini, 2007 – Vicentini, C.B., Romagnoli, C., Reotti, E., Mares, D.J. (2007). *Agric. Food Chem.,* 55.

Wada et al., 2015 – *Wada, H., Hyun, H., Vargas, C., Gravier, J., Park, G., Gioux, S., Frangioni, J.V., Henary, M., Choi, H.S.* (2015). Pancreas-Targeted NIR Fluorophores for Dual-Channel Image-Guided Abdominal Surgery. *Theranostics,* 5, 1–11.

Wade, 1999 – *Wade, Jr.LG.* (1999). Organic Chemistry 4th ed. Pearson Educ. (Prentice Hall, Upper Saddle River, New Jersey 07458, USA), pp. 500-538.

Wade, 1999a – *Wade, Jr.LG.* (1999). Organic Chemistry 4th ed. Pearson Educ. (Prentice Hall, Upper Saddle River, New Jersey 07458, USA), pp. 544-560.

Appendix

Table 1:Characterization of the prepared compounds 3, 4, (5a-c) and (6a-c)

Comp No.	Nature of products			Molecular formula (M.Wt)	Analysis%						Absorption spectra in 95%ethanol	
	Colour	yield %	MP C°		Calculated			Found			λ_{max}(nm)	ε_{max} ($mol^{-1}.cm^2$)
					C	H	N	C	H	N		
3	Brown crystals	40	230	$C_{14}H_{11}N_3O_2$(253)	66.4	4.35	16.6	66.22	4.28	16.55	.....	.....
4	Dark brown crystal	57	160	$C_{18}H_{21}N_3O_2I_2$(565)	38.2	3.72	7.43	38.18	3.7	7.41	.....	.....
5a	Red	50	155	$C_{25}H_{28}N_4O_2I_2$(670)	44.78	4.18	8.36	44.75	4.15	8.32	385, 520	12820, 5750
5b	Red	55	165	$C_{29}H_{30}N_4O_2I_2$(720)	48.33	4.17	7.78	48.3	4.15	7.77	410, 540	11030, 3690
5c	Red	65	175	$C_{29}H_{30}N_4O_2I_2$(720)	48.33	4.17	7.78	48.29	4.13	7.75	395, 530	10670, 5840
6a	Deep red	55	160	$C_{32}H_{35}N_5O_2I_2$(775)	49.55	4.52	9.03	49.52	4.5	9.01	390, 530	13510, 6360
6b	Deep red	57	170	$C_{40}H_{39}N_5O_2I_2$(875)	54.86	4.46	8	54.84	4.43	7.98	420, 550	12400, 6380
6c	Deep red	59	162	$C_{40}H_{39}N_5O_2I_2$(875)	54.86	4.46	8	54.83	4.41	7.96	400, 540	14600, 6350

Table 2:Characterization of the prepared compounds 7, (8a-c) and (9a-c).

Comp No.	Nature of products			Molecular formula (M.Wt)	Analysis%						Absorption spectra in 95% ethanol	
	Colour	yield %	MP C°		Calculated			Found			λ_{max}(nm)	ε_{max} ($mol^{-1}.cm^2$)
					C	H	N	C	H	N		
7	Deep brown	75	200	$C_{28}H_{41}N_3O_6I_2$(769)	43.69	5.33	5.46	43.65	5.31	5.43	.....	.....
8a	Red	45	175	$C_{32}H_{40}N_4O_4I_2$(798)	48.12	5.01	7.02	48.9	5	7.01	440, 570, 630	13770, 7140, 2940
8b	Violet	57	185	$C_{36}H_{42}N_4O_4I_2$(848)	50.94	4.95	6.6	50.91	4.91	6.57	450, 520, 650	15730, 19470, 2400
8c	Deep red	50	180	$C_{32}H_{40}N_4O_4I_2$(798)	48.12	5.01	7.02	48.9	5	7	450, 490, 580, 640	12720, 12740, 7070, 3140
9a	Deep red	49	177	$C_{36}H_{39}N_5O_2I_2$(827)	52.24	4.72	8.47	52.21	4.69	8.43	440, 490, 580, 640	14280, 15040, 7330, 3630
9b	Deep violet	61	195	$C_{44}H_{43}N_5O_2I_2$(927)	56.96	4.64	7.55	56.91	4.61	7.52	470, 500, 520, 560, 660	20860, 22150, 22600, 23600, 6000
9c	Deep red	52	185	$C_{36}H_{39}N_5O_2I_2$(827)	52.24	4.72	8.47	52.22	4.69	8.43	450, 490, 590, 650	13830, 12120, 7060, 4000

Table 3. IR and ^{1}H NMR (Mass) Spectral Data of the Prepared Compounds

Comp. No.	IR Spectrum (KBr, Cm^{-1})	^{1}H NMR Spectrum (DMSO, δ); & (Mass data).
3	695, 753 (monosubstituted phenyl). 1030, 1116 (C—O—C cyclic). 1303, 1365 (C—N). 1493, 1404 (C═N). 1603 (C═C).	2.2-2.4 (m, 3H, CH_3 of position 5). 3.4 (b, 3H, CH_3 of position 3). 7.2-8 (m, 5H, aromatic). M^+: 253
4	693, 753 (monosubstituted phenyl). 1116 (C—O—C cyclic). 1308 (C—N). 1495, 1405 (C═N). 1604 (C═C). 2917 (quaternary salt).	1.2-1.6 (m, 6H, $2CH_3$ of positions 4, 6). 1.8-2.1 (m, 4H, $2CH_2$ of positions 4, 6). 2.2-2.4 (m, 3H, CH_3 of position 5). 3.28 (s, 3H, CH_3 of position 3). 7.2-8 (m, 5H, aromatic). M^+: 565

5b	691, 756 (monosubstituted phenyl). 813, 904 (o.disubstituted phenyl). 1123 (C—O—C cyclic). 1323, 1363 (C—N). 1495 (C═N). 1597 (C═C). 2924 (quaternary salt).	1.2-1.7 (m, 6H, $2CH_3$ of positions 4, 6). 1.8-2.1 (m, 4H, $2CH_2$ of positions 4, 6). 2.2-2.4 (m, 3H, CH_3 of position 5). 2.7-3.1 (m, 3H, CH_3 of N-quinolinium). 3.4-3.8 (m, 2H, CH_2 of N-quinolinium). 4.8-5.2 (m, 1H, —CH═). 6.7-8.7 (m, 11H, aromatic + heterocyclic).
6b	692, 757 (monosubstituted phenyl). 815, 905 (o.disubstituted phenyl). 1122 (C—O—C cyclic). 1324, 1364 (C—N). 1496 (C═N). 1598 (C═C). 2922, 2858 (quaternary salt).	1.2-1.6 (m, 6H, $2CH_3$ of positions 4, 6). 1.8-2.3 (m, 4H, $2CH_2$ of positions 4, 6). 3.0 (b, 3H, CH_3 of N-quinolinium). 3.3 (b, 2H, CH_2 of N-quinolinium). 4.8-5.2 (m, 2H, 2 —CH═). 6.7-8.7 (m, 17H, aromatic + heterocyclic).
7	698, 750 (monosubstituted phenyl). 1115, 1173 (C—O—C cyclic). 1366, 1305 (C—N). 1494, 1405 (C═N). 1602 (C═C). 2861 (quaternary salt).	1.2-1.9 (m, 8H, $2CH_3$ of position 4, 6 + 2—CH of diethoxyethyl). 2-2.2 (m, 4H, $2CH_2$ of position 4, 6). 2.3-2.4 (m, 12H, $4CH_3$ of diethoxyethyl). 3.4 (b, 12H, $6CH_2$ of diethoxyethyl). 7.2-8 (m, 5H, aromatic). M^{+2}: 771
8b	614, 687 (monosubstituted phenyl). 755 (o.disubstitute phenyl). 1156 (C—O—C cyclic). 1263 (C—O ether). 1317, 1373 (C—N). 1492 (C═N). 1631 (C═C). 2923 (quaternary salt).	1.2-1.7 (m, 7H, $2CH_3$ of positions 4, 6 + 1—CH of diethoxyethyl). 1.8-2.2 (m, 4H, $2CH_2$ of positions 4, 6). 2.3-2.4 (m, 6H, $2CH_3$ of diethoxyethyl). 2.6 (m, 6H, $3CH_2$ of diethoxyethyl). 3.0 (b, 3H, CH_3 of N-quinolinium). 3.3 (b, 2H, CH_2 of N-quinolinium). 4.4-5 (m, 3H, 3—CH=). 7-8.4 (m, 11H, aromatic + heterocyclic).
9b	622, 688 (monosubstituted phenyl). 754, 999 (o.disubstituted phenyl). 1157 (C—O—C cyclic). 1317, 1373 (C—N). 1486 (C═N). 1636 (C═C). 2919 (quaternary salt).	1.2-1.7 (m, 6H, $2CH_3$ of positions 4, 6). 1.9-2.3 (m, 4H, $2CH_2$ of positions 4, 6). 2.7-3 (m, 6H, $2CH_3$ of N-quinolinium). 3.2-3.4 (m, 4H, $2CH_2$ of N-quinolinium). 4.4-5 (m, 6H, 6—CH═). 7-8.7 (m, 17H, aromatic + heterocyclic).

Table 4. Antimicrobial activity of some selected prepared compounds

Sample		Inhibition zone diameter (mm / mg sample)			
		Bacillus Subtilis (G^+)	**Escherichia Coli (G^-)**	**Pseudomonas Aeruginosa (G^-)**	**Staphylococcus Aureus (G^+)**
Control: DMSO		0.0	0.0	0.0	0.0
Standard: Antibacterial Agent	**Tetracycline**	30	32	31	28
	Ampicillin	20	22	17	18
3		0.0	9	0.0	9
4		0.0	9	9	10
5b		0.0	0.0	9	0.0
6a		13	16	17	13
6b		0.0	9	9	11
6c		9	11	11	11
7		0.0	0.0	0.0	0.0
9a		11	16	15	12
9b		0.0	12	12	10
9c		0.0	12	12	9

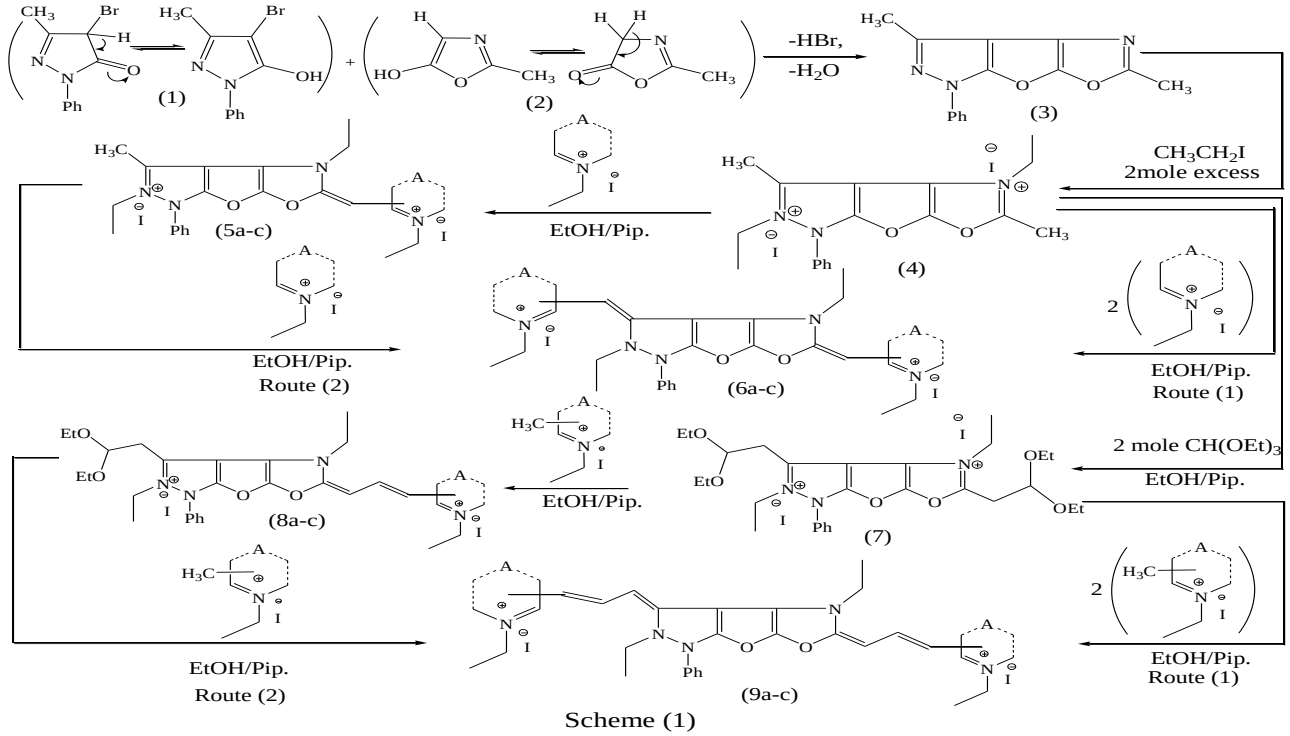

Scheme (1)

Synthesis Strategy of the prepared compounds (5a-c), (6a-c), (8a-c), and (9a-c).

Substituents in scheme (1):

(5a-c), (6a-c): A = 1-ethyl pyridinium-4-yl salt (a), 1-ethyl quinolinium-4-yl salt (b), 2-ethyl isoquinolinium-1-yl salt (c).

(8a-c), (9a-c): A = 1-ethyl pyridinium-2-yl salt (a), 1-ethyl quinolinium-2-yl salt (b), 1-ethyl pyridinium-4-yl salt (c).

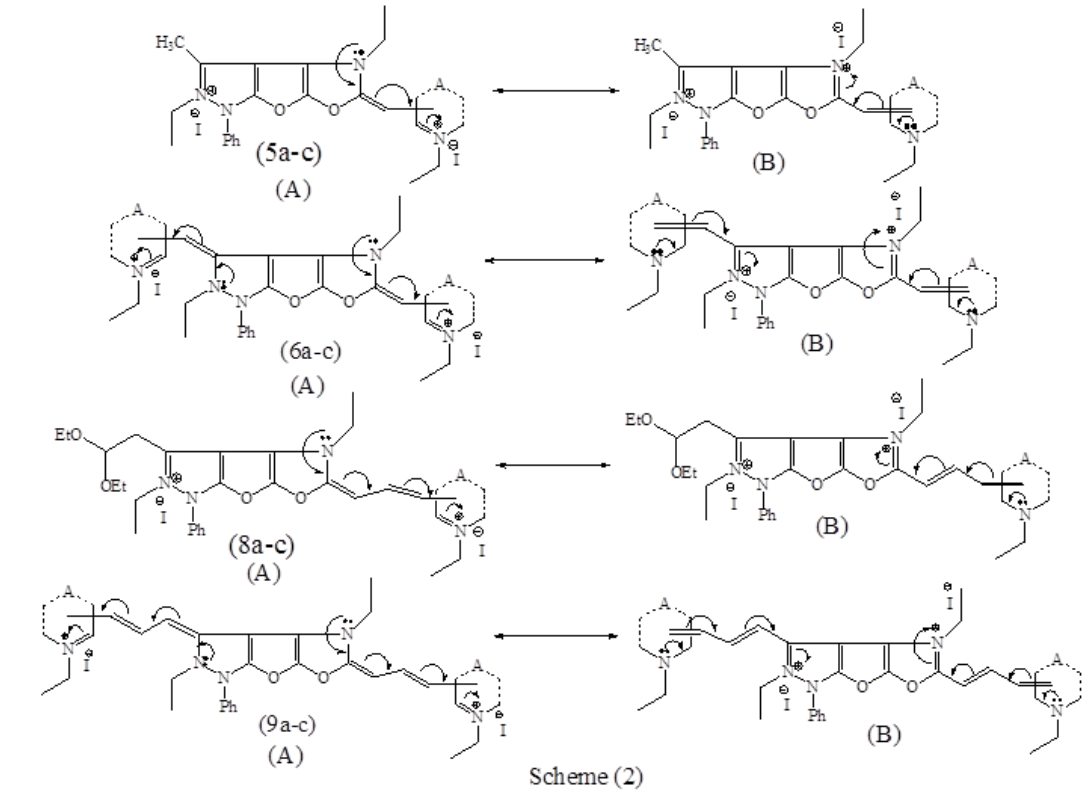

Scheme (2)

Colour intensity and / or the electronic charge transfer pathways illustration of the synthesized cyanine dyes (5a-c), (6a-c), (8a-c), and (9a-c).

Published in the Slovak Republic
European Journal of Molecular Biotechnology
Has been issued since 2013.
E-ISSN: 2409-1332
2018, 6(2): 96-106

DOI: 10.13187/ejmb.2018.2.96
www.ejournal8.com

The Effect of Substrate Nature Gas Diffusion Layer PTFE Content and Catalyst Layer Platinum Loading on the Performance of Low Temperature Proton Exchange Membrane Fuel Cell

A. Tounsi [a, *], M.El idrissi [b]

[a] Moulay Slimane University, Morocco
[b] Chouaïb Doukkali University, El Jadida, Morocco

Abstract

The nature of the substrate, the content of Polytetrafluoroethylene (PTFE) and platinum (Pt) loading are the key factors to determine the heat transfer characteristics and hydrophobicity of the gas diffusion layer (GDL) and to enhance hydrogen oxidation and oxygen reduction kinetics which directly affect the performance of the proton exchange membrane fuel cell (PEMFC).

Here, we carried out-of-cell studies of the effect of the nature of the substrate, carbon black and PTFE loading in the GDL on the cell performances. Performances of double layered cathodes are evaluated from the current density-voltage (i-V) characteristics of the single cell. In addition, the behaviour of Pt loading on the amount of electroactive catalyst area is studied using cyclic voltammetry (CV).

Keywords: polymer electrolyte membrane fuel cell, Membrane electrode assembly, Nafion®, Gas diffusion layer.

1. Introduction

Modern fuel cell shows great promise for research and development technology for more clean and effective energy sources. A fuel cell converts hydrogen and oxygen to electricity directly by an electrochemical reaction. Among several fuel cell systems, PEMFC is a popular choice for mobile, portable and stationary power systems such as for automobiles and cellular phones. Compared with other fuel cell systems they have the advantage of high-power densities at relatively low operating temperatures small and lightweight (Wu et al., 2016; Chen et al., 2016).

A PEMFC consists of two porous electrodes: an anode, to which hydrogen fuel is supplied, a cathode to which oxygen or air is supplied, and a perfluorosulfonic acid electrolyte membrane that permits the flow of protons from the anode to cathode. Nafion® produced by DuPont is one of the most popular polymer electrolyte films today (Young et al., 2017).

The porous GDL in a PEMFC consists of a thin layer of carbon black mixed with PTFE that is coated onto a sheet of macro-porous carbon backing cloth. This GDL ensures that reactants effectively diffuse to the CL. In addition, the GDL is the electrical conductor that transports electrons to and from the GDL. Although the diffusion layer is an apparently slight component in a fuel cell, it has been shown that varying the composition of the diffusion layer can lead to substantial improvements in the performance of the cell (Deke et al., 2018). The improvements reported relating to the thickness and the porosity of the layer which functions as the electrical

* Corresponding author
E-mail addresses: idrissi_82@hotmail.fr (A. Tounsi)

contact resistance and rejects liquid water from the membrane electrode assembly (MEA) (Sassin et al., 2016).

In H_2/O_2 (air) PEMFC, platinum has proven to be the best catalyst for both anodic and cathodic reactions. In order to lower the platinum loading and to increase further the electrode performance, it is necessary to prepare an electrode with high platinum utilization. The electrodes with the platinum layer at the front surface have been developed because the structure of the electrode determines the electrochemically active surface areas (EAS) in the fuel cell (Łukaszewski et al., 2016). The use of a solid polymer as an electrolyte causes the problem of non-active catalysts in the electrode. Therefore, the Nafion® solution is impregnated on the electrode surface to extend the catalytic reaction area by forming passages of ionic transfer (Jacobs et al., 2016).

In this work, GDLs were made of carbon paper or prepared by applying porous GDLs to each face of a carbon cloth support. The CL was prepared using a simple method that consists of mixing supported catalyst with Nafion® solution and water and spraying the ink so obtained onto the GDL. This method was not only simpler, safer and more economical, but also achieved better performance.

Performances of double layered cathodes were evaluated from the i-V characteristics of a single cell. The influence of platinum loading on the amount of electroactive catalyst area is studied using CV.

2. Experimental details

2.1. Reagents

Commercial electrocatalysts powders (E-TEK Johnson Matthey) consisting of 20 wt. % platinum nanoparticles supported by Vulcan XC-72 were chosen here because of their current use in PEMFC technology. They offer rather well-defined catalytic particle sizes (2.5-3 nm) and specific surface areas. The Nafion® solution is a 5 w/w 1100 EW solution from DuPont. Pure Vulcan XC-72 (Cabot), was used to prepare mixtures with E-TEK powders. High purity nitrogen gas and 99.999 % pure oxygen, pure hydrogen, and air gas were used.

2.2. Electrode preparation

The electrode was composed of a gas diffusion layer and a catalyst layer. The GDL was prepared on wet-proofed carbon cloth with PTFE. It is obtained by filing the carbon cloth with a mixture composed of carbon powder (Vulcan XC-72) and PTFE 30 wt. % and isopropyl alcohol (IPA). The viscous mixture was screen-printed on to the wet-proofed carbon cloth and then dried for 24 hours.

The mixture composing the CL (ink of Pt/C -20 wt. % Pt on Vulcan XC-72, IPA, PTFE 30 wt. % and 5 wt. % Nafion® solution was then sprayed on one side of the GDL. The spraying method allows easy control of the platinum ratio on the electrodes.

2.3. Electrode and membrane assembly

Nafion® 117 polymer electrolyte membrane was treated with boiling H_2O_2 and H_2SO4 to remove organic and metallic impurities for 1 h respectively and then washed in distilled water for 1 hour (Kaufman et al., 2002; Giorgi et al., 1998; Jordan et al., 2000). For the performance evaluation, an anode and a cathode are re-impregnated with electrolyte Nafion® solution in order to obtain loadings of approximately 0,5 mg/cm² and then hot-pressed on each side of the proton exchange membrane at 140 °C under 50 kg/cm² for 5 minutes.

2.4. Test cells and electrochemical instrumentation

The obtained EMAs were inserted in the fuel cell hardware consisting of two graphite blocks with parallel flow field channels for the reactants, two copper current collectors and an end plate assembly.

Two types of single cells test fixture (5 and 50 cm²) purchased from Globetech Inc. (USA) were used in this study. We note that on the 5 cm² cell test (Figure 1) anodic and cathodic potentials are separately determined thanks to an internal reference consisting of a platinum wire which relates to a piece of electrode stuck on the membrane at the anode side. The reference electrode is supplied with hydrogen gas by a derivation in the cell. This single cell is incorporated in a test station fabricated in our laboratory with all its peripheral components (temperature controller, humidification, flow meter, pressure regulator, etc...). During the performance evaluation the fuel cell is connected in series with power supplies for their operations under galvanostatic load and cell voltages, as well as half-cell potentials, were recorded versus current

densities. Measurements were made at 80 °C and under 3-atmosphere pressure of H_2 at the anode and 5-atmosphere pressure O_2 or air at the cathode. The humidification of the anode/cathode gas streams was realized by diverting the streams through heated water-filled bottles that were usually kept at 95 °C for H_2 and O_2 or air. We impose on the cell a current density of 200 mA/cm² during 20 hours. The i-V density characteristic curves were then plotted using a dc Electronic Load for every electrode model. Cyclic voltammetry (CV) was carried out with a Wenking potentiostat-galvanostat in order to determine the electrochemically-active surface area (ESA). For CV studies, nitrogen was passed through the 5 cm² test electrode and hydrogen was passed through the counter electrode chamber. The counter electrode was also used as the reference electrode because of the negligible overpotential for hydrogen oxidation and reduction on platinum. The potential was then scanned between 100 and 1400 mV versus the reversible hydrogen electrode (RHE) at a scanning rate of 50 mV/s. The ESA of the Pt catalyst was evaluated from the voltammogram by dividing the charge is expressed in units of microcoulomb that corresponded to the area under the hydrogen desorption region by 210 µC (Srinivasan et al., 1990; Ticianelli et al., 1988 and Giorgi et al., 1999).

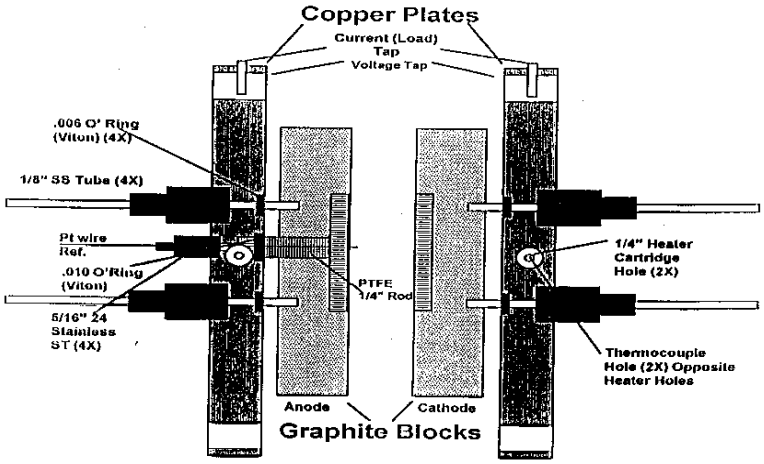

Fig. 1. Schematic diagram of the single cell test fixture (5 cm²) (Globtech Inc)

The experimental roughness factor (RF_{exp}) was calculated by dividing the ESA by the geometric area (5 cm²) of the electrode. Knowing that the surface determined by the adsorption of CO is 112 m² per gram of platinum (for Vulcan XC-72 - 20 wt.% in platinum) the theoretical roughness factors RF_{th} of an electrode according to its load in catalyst L_{Pt} are given by:

$$RF_{th} = 1120(cm^2/mg\ Pt) \times L_{Pt}(mg/cm^2)$$

Utilization of the Pt catalyst was evaluated by dividing the experimental roughness factor (RF_{ex}) of the electrode by the theoretical one (RF_{th}) (Watanabe et al., 1995). From both roughness factors, theoretical and experimental, it is possible to estimate the platinum utilization (η_{Pt}) by:

$$\eta_{Pt} = 100 \times \frac{RF_{ex}}{RF_{th}}$$

3. Results and discussion

3.1. Preliminary test

In order to qualify cell test under our experimental conditions, we studied the performances of cells exclusively made with commercial E-TEK electrodes. These electrodes containing Pt loading of 0,4 mg/cm² will be afterward chosen as "reference" for the present study. The polarization curves recorded with both 5 and 50 cm² cells are recorded in Figure 2. We note a good concordance of the results obtained with two types of a single cells test fixture.

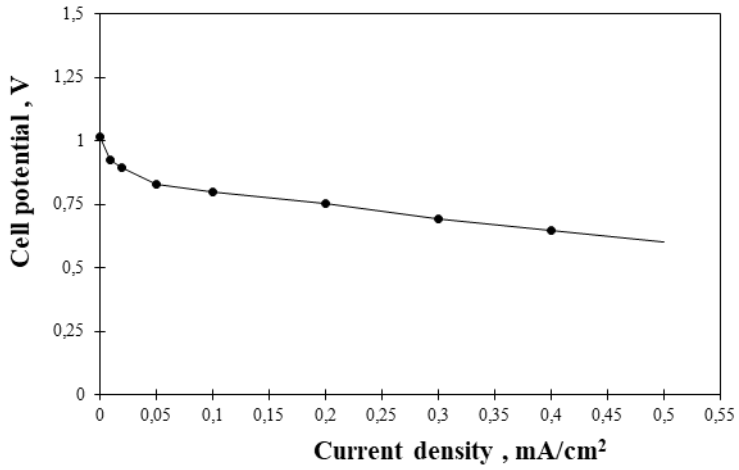

Fig. 2. Polarization curves of 5 cm² (-) and 50 cm² (•) O_2 E-TEK /Nafion® / H_2 E-TEK PEMFCs

Figure 3 gives polarization curves of the same cells supplied with air. The influence of the partial pressure of oxygen is appreciably identical in both 5 and 50 cm² electrode surfaces.

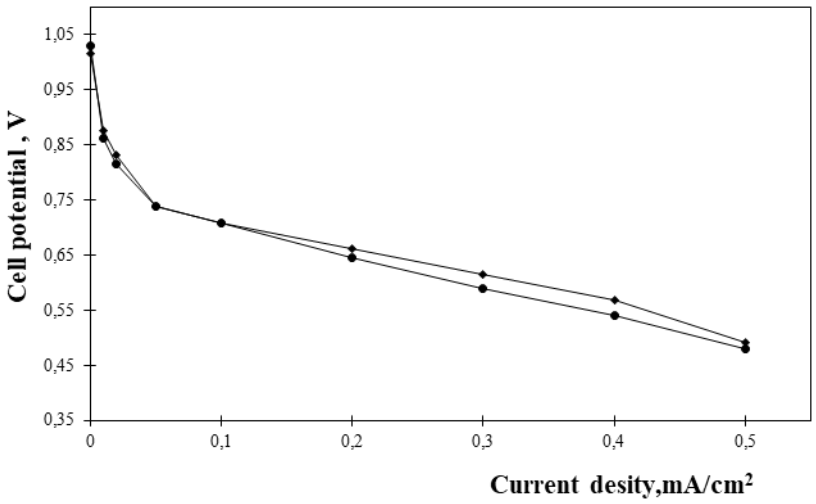

Fig. 3. Polarization curves of 5 cm² (♦) and 50 cm² (•) air E-TEK /Nafion® / H_2 E-TEK PEMFCs

Figure 4 giving anodic and cathodic partial performances show that the biggest party of the cell polarization is due to cathode kinetics.

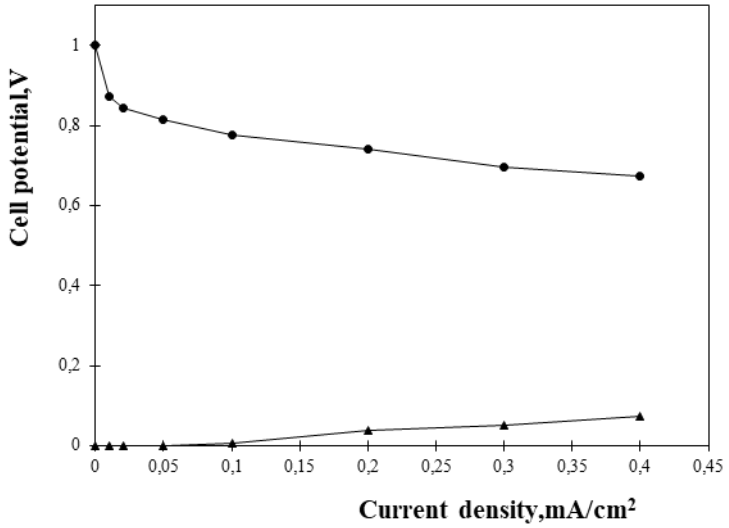

Fig. 4. 5 cm² O_2 E-TEK /Nafion® / H_2 E-TEK PEMFC performances.
(•) cathodic polarization curve; (▲) anodic polarization curve

3.2. Gas diffusion layer

3.2.1. Effect of substrate

The effect of the substrate on the PEMFC performance using PWB3 cloth and Toray paper is shown in Figure 5. As can be seen, in H_2/O_2 operation, the best cell performance was obtained with PWB3 cloth. The characteristics of the different backings differ with respect to the pore size and the grade of hydrophobicity reached by impregnating the backing with PTFE-suspension. Generally, a compromise between unhindered gas access (large, hydrophobic pores) and removal of product water (hydrophilic pores, problems of condensing or flooding the electrode) must be found. Large pores, on the one hand, provide a "free barrier" gas access. On the other hand, at the interface between the hydrophobic backing and the hydrophilic active layer the pores will probably resist the intrusion of water and a droplet will be formed. The larger the pore size, the greater is the expected size of the droplet and the reactant diffusion barrier, whereas in case of micropores only very small droplets are formed (Sasikumar et al., 2004) which can escape through the pores because of capillary forces. Dealing with the PTFE content one faces the same conflict between a highly hydrophobic layer, which is expected to provide unhindered gas access and the fact that water cannot be efficiently removed through the hydrophobic pores consequently flooding the active layer.

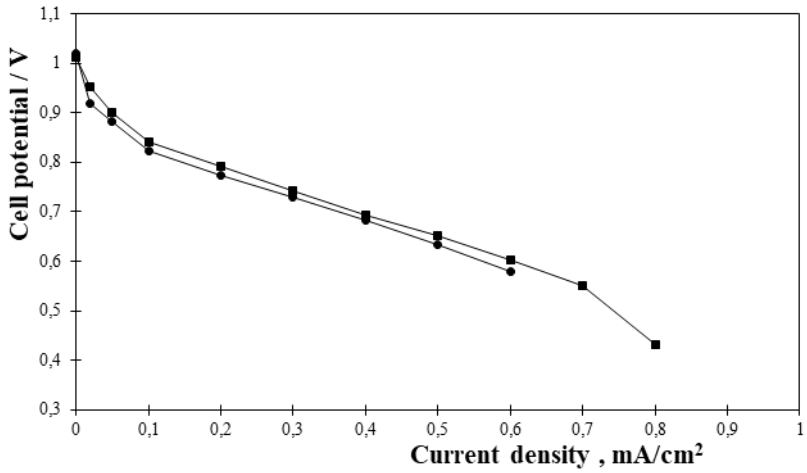

Fig. 5 Effect of the kind of substrate on the performance of O_2 /Nafion® / H_2 E-TEK PEMFC.
(■) PWB3 cloth; (•) Toray paper

3.2.2. Influence of carbon black

Using PWB3 as a substrate, we studied the influence of the powder placed in the GDL. The three carbon powder types investigated were Black Pearls 2000, Vulcan XC-72 (oil-furnace carbon black) and Shawinigan (acetylene-black) carbon powder (Bevers et al., 1996).

Black Pearls 2000 differs essentially from Vulcan XC-72 by its high specific conductivity and very high specific surface. Shawinigan Black also presents a very good specific electric conductivity and a structure getting closer very strongly to some graphite. Figure 6 shows cathode performances which GDL were prepared with these various products. We found that an electrode featuring Vulcan carbon powder performed substantially better than an electrode containing Shawinigan carbon powder and lower cell performances are obtained with acetylene black.

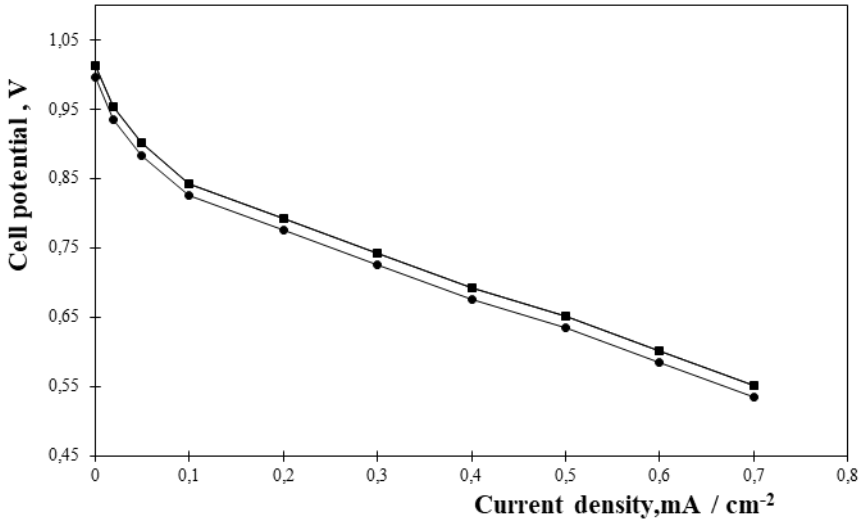

Fig. 6. O_2 /Nafion® / H_2 E-TEK PEMFCs PEMFC performances. GDLs were prepared with : (♦) Vulcan XC72 ; (■) Black pearles 2000 and (•) Shawinigan Black

3.2.3. Polytetrafluoroethylene (PTFE) content

Cell performances according to different PTFE loading in GDL of the cathode are given in Figure 7. The loading of the hydrophobic material in the GDL affects the mass transport properties of the electrode and thus the cell activity. We can note that at low current densities (lower than 0.25 A/cm²) higher cell voltages values are obtained with cell corresponding to 10 % wt. PTFE in the GDL. These best performances are attributed to a good hydration balance of the membrane obtained thanks to the retro diffusion of the water produced in the cathode. This one remains in great quantities, thanks to the partial hydrophobic character of this GDL. At high current densities, this tendency is inverted.

Figure 7 shows the effect of PTFE loading on the current density at 0.5 V. The maximum cell performance is obtained at about 30 % wt. PTFE. This behavior results from the effects of gas diffusion and ionic resistance.

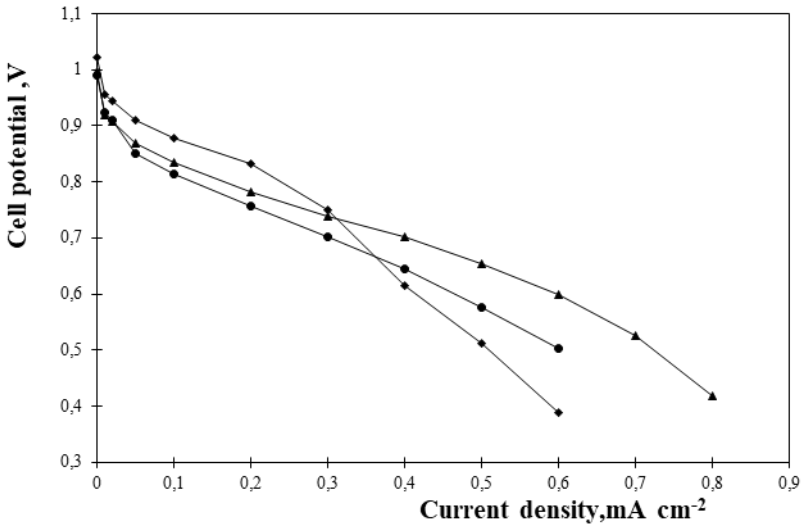

Fig. 7. O_2 /Nafion® / H_2 E-TEK PEMFC performances.
GDLs contain: (♦) 10 % wt. PTFE ; (▲) 30 % wt. PTFE ; (●) 50 % wt. PTFE

These two phenomena related to the transport of water depend greatly on the PTFE loading. Dependence of current density on polytetrafluoroethylene (PTFE) content of GDL given in Figure 8, shows that a maximum cell performance at 0.5 V is obtained at about 30 % wt. PTFE. It seems that the lower performance of cathodes containing 10 % and 50 % wt. PTFE is caused by its flooding and the increased ionic strength of the membrane and the electronic resistance of the electrode, respectively.The type of GDL material sample with 30 % corresponds certainly to a good specific electric conductivity and reinforced the hydrophobic character of the GDL (Passalacqua et al., 1998).

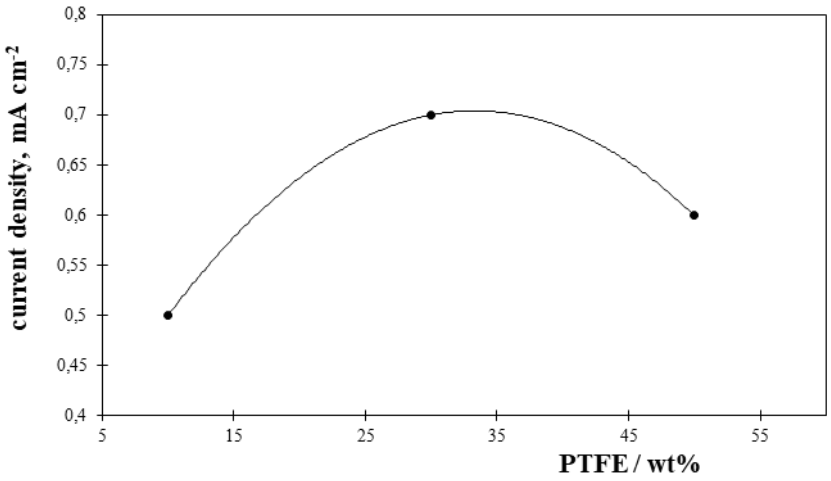

Fig. 8. Dependence of current density on polytetrafluoroethylene (PTFE) content of the GDL at cell voltage 0,5 V

3.3. Catalytic layer

Large area electrodes of about 500 cm² were prepared according to the manufacturing method described above, then samples of 5 cm² and 50 cm² were cut and tested. Figure 9 giving polarization curves of a 50 cm² and à 5 cm² single H_2/O_2 cell shows a very good reproducibility of the performances.

The thickness of the CL should be proportional to the quantity of catalyst as far as the structure does not change. The variation of this thickness is realized by the pulverizing of various quantities of a mixture (ink of Pt/C, IPA PTFE, and Nafion®) (Antonili et al., 2002).

Using a 5 cm² H_2/O_2 single PEMFCs were tested and polarization curves are plotted in Figure 9 for various platinum loading. The utilization of Pt catalyst can be provided by variation of current density at 0,65 V according to platinum loading.

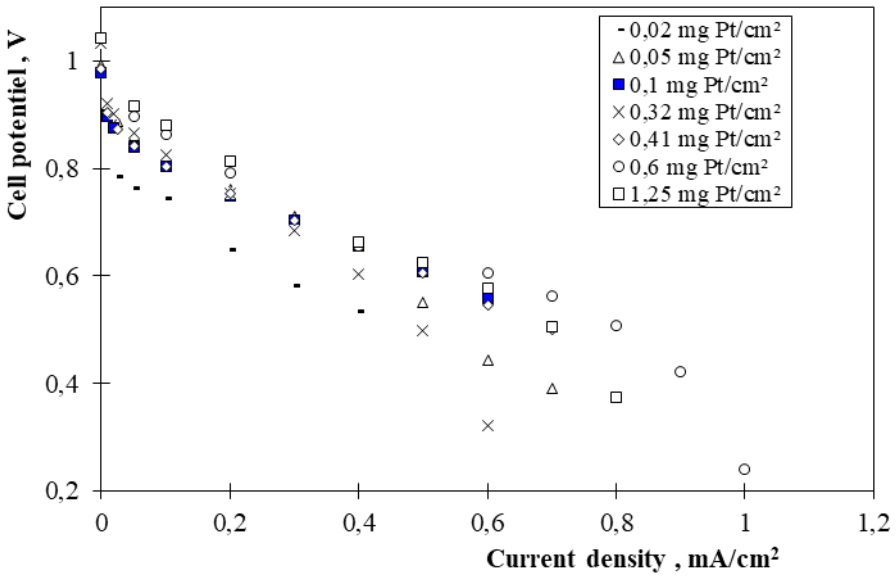

Fig. 9. (O_2 electrode/Nafion/H_2 E-TEK) cell performances for cathodic CL prepared using various Pt caralyst loading

The curve plotted in Figures 10a, 10b shows that it is possible to reduce catalyst loading close to 0.2 mg/cm² without changing significantly cell performances.

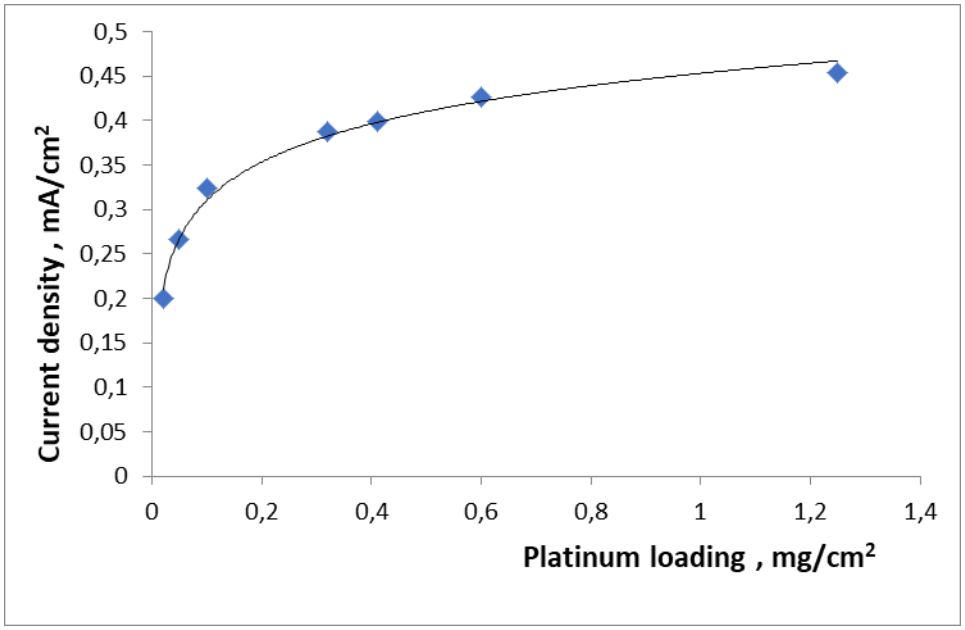

Fig. 10a. Dependence of current density on Pt catalyst loading of the cathodic CL at 0,75 V.

The electrochemically active surface area in CL has been evaluated by cyclic voltammogram studies and typical cyclic voltammogram with a scan rate of 50 mV/s of a cathode with 0,54 mg/cm² loading is given in Figure 10b.

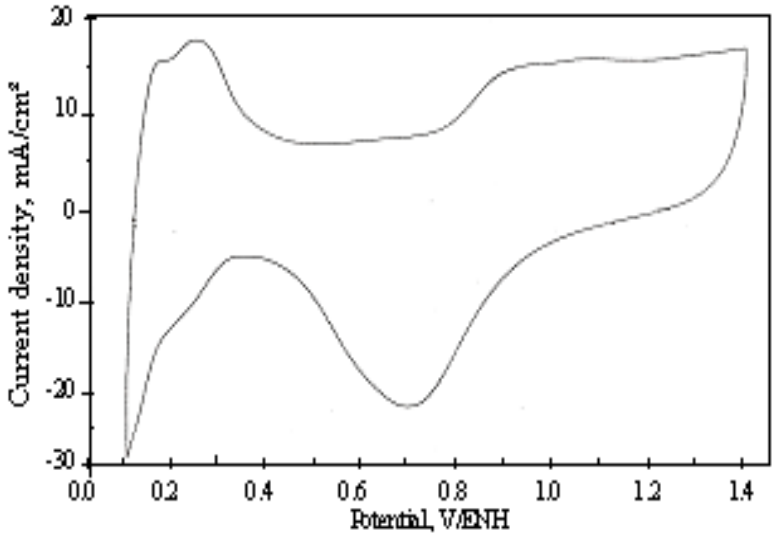

Fig. 10b. Typical cyclic voltammogram at a scan rate of 50 mV/s

The really active surface so determined is that of all the particles in ionic and electronics contact with the membrane and the support.

Figure 11 shows that the variation of RF_{th} according to L_{Pt} is a right-hand side passing by the origin and of equal hillside in 1120 cm² of platinum per mg of catalyst. On the same figure, this right-hand side is compared with that of the experimental roughness factor RF_{ex} obtained by CV. At lower platinum loads than 0,1 mg/cm² the experimental points are closer to the theoretical right-hand side. Beyond a Pt loading of 0,4 mg/cm² the experimental roughness factors go away from the theoretical right-hand side. The difference between both curves is evaluated the Pt utilization.

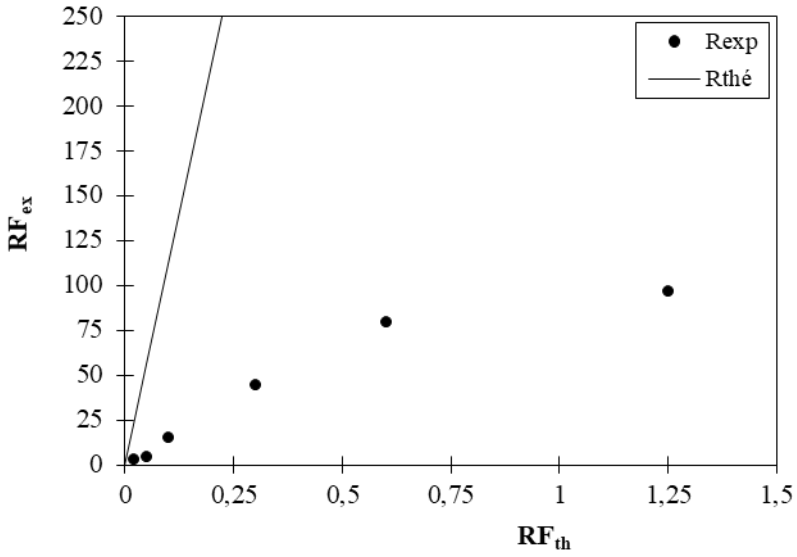

Fig. 11. Dependence of theoretical and experimental roughness factor on platinum loading in the active layer of the oxygen electrode

The dependence of the Pt utilizationon its loading plotted in Figure 12 shows that $_{Pt}$ passes from a constant value of 14 % for L_{Pt} < 0,4 mg/cm² to 8% for L_{Pt}> 1,25 mg/cm². For platinum loadings higher than 0,4 mg.cm^{-2}, the catalyst particles are not completely accessible to the protons transported through the electrolyte incorporated in the catalytic layer. It is thus not interesting to manufacture electrodes containing Ptloadings higher than 0,45 mg.cm^{-2}.

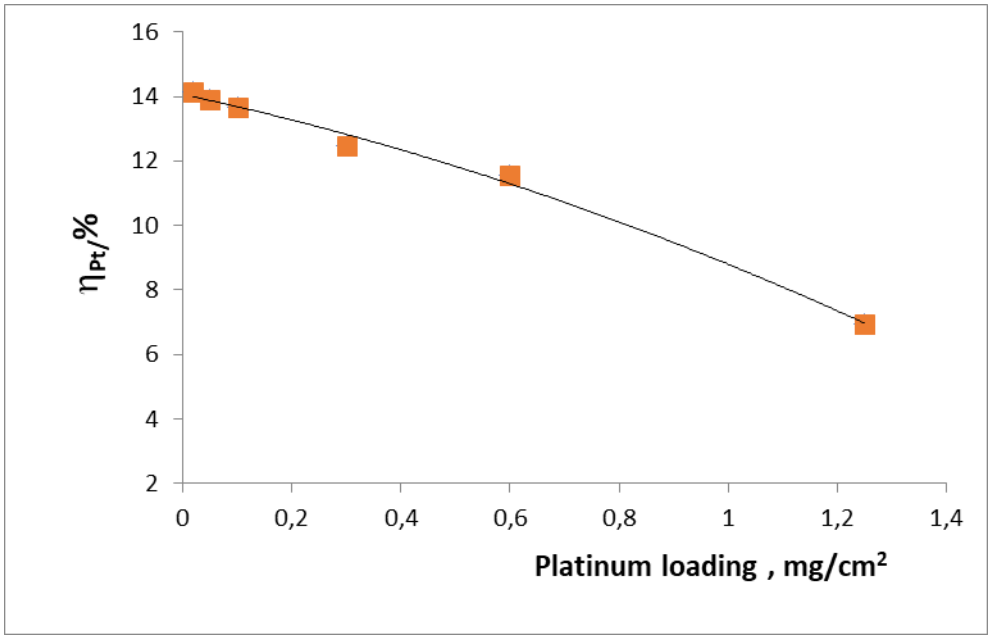

Fig. 12. Dependence of platinum utilization on its loading in the active layer of the oxygen electrode

4. Conclusion

The influence of substrate nature, carbon black, PTFE content in gas diffusion layer and catalyst layer platinum loading on the performance of PEMFC was investigated. The results presented show that:

1. The best cell performance was obtained using PWB3 cloth.
2. Using PWB3 as substrate electrode featuring Vulcan carbon powder performed substantially better than an electrode containing Shawinigan carbon powder and lower cell performances are obtained with acetylene black.
3. It is possible to reduce catalyst loading close to 0.2 mg/cm² without changing significantly cell performances. We note that for platinum loadings higher than 0.4 mg/cm², the catalyst particles are not completely accessible to the protons transported through the electrolyte incorporated in the catalytic layer.

5. Conflict of Interest

The authors declare that there is no conflict of interests regarding the publication of this paper. Also, they declare that this paper or part of it has not been published elsewhere.

References

Chen et al., 2016 – *Chen, T., Liu, S., Zhang J., Tang M.* (2016). Study on the characteristics of GDL with different PTFE content and its effect on the performance of PEMFC. *Int. J. Heat Mass Transfer,* 128, 1168-1174.

Wu et al., 2016 – *Wu, H.* (2016). A review of recent development: transport and Jacobs, C. J. Influence of catalyst ink mixing procedures on catalyst layer properties and in-performance modeling of PEM fuel cells, Appl. Energy 165, 81–106.

Young et al., 2017 – *Birss, V., Elsawy, E., Ketabi, S., Keyvandar, P., Li, X., Young, J.* (2017). Handbook of Industrial Chemistry and Biotechnology. (Eds: J.A. Kent, T.V. Bommaraju, S.D. Barnicki), 13thed., Springer, Cham, P. 1733.

Deke et al., 2018 – *Dekel, D.R.* (2018). Review of cell performance in anion exchange membrane fuel cells. *Journal of Power Sources,* 375, 158-169.

Sassin et al., 2016 – *Sassin, M.B. et al.* (2016). Impact of compressive stress on MEA pore structure and its consequence on PEMFC performance. *Journal of The Electrochemical Society*, 163.8, F808-F815.

Łukaszewski et al., 2016 – *Łukaszewski, M., Soszko., M., Czerwiński, A.* (2016). Electrochemical methods of real surface area determination of noble metal electrodes–an overview. *Int. J. Electrochem. Sci*, 11, 4442-4469.

Jacobs et al., 2016 – Situ PEMFC performance. Diss. University of Cape Town.

Kaufman et al., 2002 – *Qi, Z., Kaufman* (2002). *A. J. Power Sources,* 109, 38.

Giorgi et al., 1998 – *Giorgi, L., Antolini, E., Pozio., A., Passalacqua, E.* (1998). *Electrochim. Acta*, 43, 3675.

Jordan et al., 2000 – *Jordan, L.R., Shukla, A.K., Behrsing T., Avery, N.R., Muddle B.C., Forsyth M.* (2000). *J. Power Sources*, 86, 250.

Srinivasan et al., 1990 – *Srinivasan, S., Manko, D.J, Koch, H., Enayetullah, M.A.* (1990). Appleby, A.J, *J. Power, Sources,* 29, 367.

Ticianelli et al., 1988 – *Ticianelli, E.A., Derouin, C.R., Srinivasan, S., Electroanal, J.* (1988). *Chem.* 251, 275.

Giorgi et al., 1999 – *Antolini, E., Giorgi, L., Pozio, A., Passalacqua, E.J.* (1999). *Power Sources,* 77, 136.

Watanabe et al., 1995 – *Watanabe, M., Igarashi, H., Yosida, K.* (1995). Electrochim. *Acta,* 40, 329.

Sasikumar et al., 2004 – *Sasikumar, G., Ihm, J.W., Ryu, H., Power, J.* (2004). *Sources*, 132, 11.

Bevers et al., 1996 – *Bevers, D., Rogers, R., von Bradke, M., Power, J.* (1996). *Sources,* 63, 193.

Passalacqua et al., 1998 – *Passalacqua, E., Lufrano, F., Squadrito., G., Patti, A., Giorgi, L.* (1998). *Electrochimica Acta,* 43, 3665.

Antonili et al., 2002 – *Antonili, E., Passos, R.R, Ticianelli, E.A. Power, J.* (2002). Sources 109, 477-482.